Experimental and Numerical Investigations of Solitary Wave-induced Non-equilibrium Scour around Structure of Square Cross-section on Sandy Berm

Erdinc Sogut[1], Tian-Jian Hsu[2], and Ali Farhadzadeh[1, †]

[1]Department of Civil Engineering, College of Engineering and Applied Sciences, Stony Brook University, Stony Brook, 11794, New York, USA.

[2]Department of Civil and Environmental Engineering, University of Delaware, Newark, DE 19716, USA.

ABSTRACT

A series of laboratory experiments and high-fidelity numerical simulations were carried out to investigate the scour induced by a solitary wave around a non-slender, vertical structure of a square cross-section on a sandy berm. Various wave and water level combinations, structure layouts, and dimensions were studied. The flow separation at the sharp edges resulted in counterclockwise rotating out-of-plane vortices that extended from the free surface to the sandy berm. These energetic vortices were found to be the primary driving mechanism of the scouring through entraining, and entrapping the sand particles into their cores, keeping them in suspension, carrying them, and releasing them as the vortices propagate along a spiral trajectory. The analyses also showed that the flow blockage by the structure could result in flow field modulation and exacerbate the scour processes. The structure dimension appeared to be the most influential factor in the scouring process, drastically altering the characteristics of the non-equilibrium scour holes. Irrespective of the structure dimension or layout, the scour depth was greater around the seaside edge of the structure while the scour width was larger on the leeside edge. The uncertainties associated with the maximum non-equilibrium scour depth were quantified via Monte Carlo simulations which showed that the impact of the structure dimension on the maximum scour depth was almost twice more significant than that of the layout. The three-dimensional (3D) Eulerian two-phase flow numerical model, SedWaveFoam, was shown to be able to simulate sediment

---

† Corresponding author
Email address: ali.farhadzadeh@stonybrook.edu (Ali Farhadzadeh)

transport and scour around sharp-edged square structure at a low Keulegan-Carpenter (KC) number.

Keywords: Foundation erosion, boundary layer, Shields parameter, Monte Carlo simulation, suspended sediment

1.INTRODUCTION

Understanding and quantification of scour around riverine and coastal structures have been a popular research topic. Scour around slender cylindrical structures has particularly received more attention (Baykal et al., 2017; Kobayashi, 1993; Kobayashi and Oda, 1995; Sumer et al., 1993, 1992; Sumer and Fredsøe, 2002; Whitehouse, 1998), mainly due to its implications for a broad range of structures from offshore platforms in the oil industry to piers and bridges in the transportation sector. However, relatively less is known about scour processes for non-slender, non-cylindrical structures. Rance (1980) investigated the wave and current-induced scour around large monopiles of various shapes where the width of the pile, D, was greater than 10% of the wavelength, L. Rance (1980) concluded that the scour depth for a structure with a square cross-section could be significantly greater than that for the structures of cylindrical and hexagonal cross-sections. Katsui et al. (1993, 1989), and Toue et al. (1993) studied the scour around large vertical piles exposed to regular waves. They identified wave-induced steady-streaming as the main driving mechanism of the scouring. To predict the bed evolution around large cylindrical piles, Saito et al. (1991) developed a numerical model which was later improved by Katsui and Toue (1993) with the implementation of a wave-current friction component. The model was limited to planar slopes and did not account for the effects of undertow currents, an important scour-inducing process on sloping bottoms (Saito and Shibayama, 1993). Kim et al. (1995) studied the scour around two large cylindrical structures and concluded that the depth and width of the scour hole depended on the number of structures, diffraction parameter (D/L), incident wave angle, and sediment size. Sumer and Fredsøe (2002) showed that, for large cylinders, the scour depth increased with the diffraction parameter, owing to the wave-induced steady-streaming. Consistent with the findings of Rance (1980), Sumer and Fredsøe (2002) reported greater scour depths around a square pile than those for a cylindrical pile under both wave and combined wave and current flow condition. Furthermore, by investigating the scour around a large cylindrical pile, Sumer and Fredsøe (2001) indicated that the scour occurs because the sediment is brought into suspension and carried away by the wave actions and that the scour depth was a function of both Keulegan-Carpenter number (KC) and diffraction parameter. Sumer and Fredsøe (2002) argued that the time scale for the establishment of an equilibrium scour around a large cylindrical pile exposed to progressive waves increased with the Keulegan-Carpenter number and diffraction parameter and decreased with the Shields parameter (θ). A study by Whitehouse (2004) on the scour of three different large marine monopile structures showed that the foundations were less susceptible to scouring in a wave-dominated regime while scour protection measures were necessary under a combined wave and current flow condition. Haddorp (2005) stated that under extreme and moderate wave conditions, the scour depth around a pile could be on the order of one and one-third the pile diameter, respectively. Qi and Gao (2014) experimentally studied the scour around a large diameter monopile by the actions of combined wave and current. They indicated that wave-induced seepage reduced the buoyant unit weight of the surrounding sand under the wave trough—also known as liquefaction—making the sandy bed more prone to scour. Furthermore, they found that because of the nonlinear interactions between waves and currents, the combined wave and current flow leads to a greater scour depth than that of waves or currents. Nakamura et al. (2008) investigated tsunami-induced local scour around a land-based square structure on a sandy bed via laboratory experiments and numerical simulations. They discovered that the maximum scour depth is a function of the inundation depth and embedment depth of the footing. The numerical simulations also revealed that effective stress is an important parameter in the development of the scour hole. McGovern et al. (2019) conducted a series of experiments on tsunami waves propagating over a sloping bottom and impinging upon a square structure on a flat erodible bed. The non-equilibrium scour depth was found to be affected by sediment slumping.

The majority of the past studies, some of which are briefly reviewed above, focus on the equilibrium scour of various types of structures under different flow conditions. Among these studies, slender structures are well-studied, leading to the development of several empirical relationships for the scour depth (Breusers et al., 1977; Raaijmakers and Rudolph, 2008; Sumer et al., 1992; Sumer and Fredsøe, 2002; Whitehouse, 1998; Zanke et al., 2011). On the other hand, less is known about the non-equilibrium scour characteristics of non-slender structures—which motivated the authors to undertake the present study. The formation and evolution of vortical structures around non-slender structures were previously studied using high-fidelity, eddy-resolving, numerical simulations, and experiments (Sogut et al., 2020, 2019; Velioglu Sogut et al., 2021). Here, the authors present the results of their experimental studies on the formation and evolution of the vortical structures under various wave and water levels, structure sizes, and layouts on a sandy berm. Moreover, the morphological evolution of the sandy berm in the vicinity of a non-slender structure with a sharp-edged square cross-section under a non-breaking solitary wave is quantified. For that purpose, the characteristics of the scour holes, i.e., depth, width, and volume, as well as the sediment deposits forming near the structure are analyzed. Because the observed non-equilibrium scouring process entails more uncertainties than the equilibrium scour, an uncertainty quantification based on the Monte Carlo simulation is presented.

To further enhance the analysis, measured data are compared with the simulation results of a high-fidelity numerical model, SedWaveFoam—a three-dimensional (3D) Eulerian two-phase flow model in the Open Field Operation And Manipulation (OpenFOAM) environment. This model is adopted for the present study because, unlike single-phase models (Baykal et al., 2017; Henderson et al., 2004; Kranenburg et al., 2013, 2012) which employ bedload/suspended load assumptions and bed shear stress models, two-phase flow models directly solve continuity and momentum equations for the sediment, water and air phases (Kim et al., 2018). The SedWaveFoam model's capability in simulating surface wave propagation together with sheet flow sediment transport enabled quantification of the wave-driven sediment transport in wave bottom boundary layer (Kim et al. 2018). This work expands the model's capability by simulating the sediment transport and scour around a sharp-edged square structure at a low KC number.

2.EXPERIMENTS

The flume experiments were conducted at Stony Brook University Coastal and Hydraulic Engineering Research Laboratory's (CHERL) integrated wave and bi-directional current flume, which is 25 m long, 1.5 m wide, and 1.5 m high. The flume is equipped with an active wave absorption system to reduce reflected wave effects. Further, a honeycomb mesh, shown in Figure 1 at the end of the wave flume, acted as a passive wave energy absorption to reduce wave reflections. The plan and side views of the experimental setup and the adopted coordinate system, as well as the three-dimensional visualization of each layout, are shown in Figure 1.

The flume experiments included two structure layouts and three combinations of wave and water depth conditions. The structures were two sharp-edged, wooden blocks, with cross-sectional dimensions 0.5 m $\times$ 0.5 m and 0.25 m $\times$ 0.25 m. The structures were placed on a mobile bed of

0.18 m thick, composed of sand with a median grain diameter of D_{50}=0.27 mm, and exposed to incident solitary waves. The heights of the solitary waves at the paddle were 10 cm, 7.5 cm, and 5 cm and propagated on the still water of 48 cm, 40.5 cm, and 33 cm deep, respectively. The main objective of this study was to assess and quantify the possible impacts of the inundated non-slender structure position on the non-equilibrium scour characteristics. Two layouts, the structure: (1) attached to the sidewall (side), and (2) positioned at the centerline (center) were considered. The side wall-attached case was assumed to represent an abutment wall subject to wave impact where the wall effect tends to influence the morphodynamic processes. Although this study was not designed to replicate a specific real-life condition, the ranges of structure dimensions and the corresponding flows may be considered having a λ=1:40 length scale according to the Froude similitude (e.g., Sumer and Fredsøe, (2002)).

2.1.Wave and Water Level

Table 1 summarizes the waves and water levels considered for the experiments. The wave specifications were selected such that the diffractions and consequently the potentials for the formation of undesired oscillations in the flume are minimized. This was achieved by employing the criterion proposed by Isaacson (1979) in which the diffraction coefficient (D/L) is presented as a function of the Keulegan-Carpenter (KC) number.

The solitary wave was assumed as a representative wave in a wave train where the distance between the two consecutive crests is the wavelength (L). Subsequently, the equivalent wave period (T) was defined as the ratio of the wavelength to the wave celerity, c, following Huang and Yuan, (2010) and Xu et al. (2019). In Table 1, the variable h_d is the water depth, H, c, and T are the wave height, celerity, and period, respectively. These variables are all the offshore quantities in front of the wave paddle. The parameter U_m represents the maximum undisturbed near-bottom flow velocity, measured at ~2 mm above the sandy berm. The Keulegan-Carpenter number is defined as $KC = U_m T/D$ where D is the width of the structure.

Table 1: Specifications of flow conditions and structure dimensions

H [m]	L [m]	h_d [m]	c [m/s]	T [s]	U_m [m/s]	D [m]	KC [-]	D/L [-]
0.100	7.63	0.480	2.39	3.20	0.49	0.50	3.14	0.66
						0.25	6.28	0.33
0.075	6.83	0.405	2.17	3.15	0.41	0.50	2.55	0.73
						0.25	5.11	0.37
0.050	6.15	0.330	1.93	3.19	0.29	0.50	1.87	0.81
						0.25	3.75	0.41

2.2.Measurements

The instrumentation and procedure of measuring the flow field and bed elevation are elaborated in the following subsections.

2.2.1. Water level and velocity measurement

Edinburgh Designs WG8USB resistive wave gauges (WG), with a sampling frequency of 128 Hz, recorded the free surface elevations at various locations in the flume, particularly around the structure. The locations of the wave gauges are marked in Figure 1.

Prior to placing the structure on the berm, the undisturbed near-bed velocity profile was measured using a Vectrino Profiler at a sampling frequency of 25 Hz. The near-bed flow velocity profile was measured along a 30 mm water column (between ~2 mm to 32 mm from the berm) at a resolution of 1 mm. Furthermore, the velocity field was measured using three Nortek Vectrino Acoustic Doppler Velocimeters (ADV) at a sampling rate of 25 Hz. The ADVs recorded the flow velocity at one-third the still water depth above the sandy bed. The positions of the WGs and ADVs are shown in Figure 1, and their coordinates are summarized in Table 2.

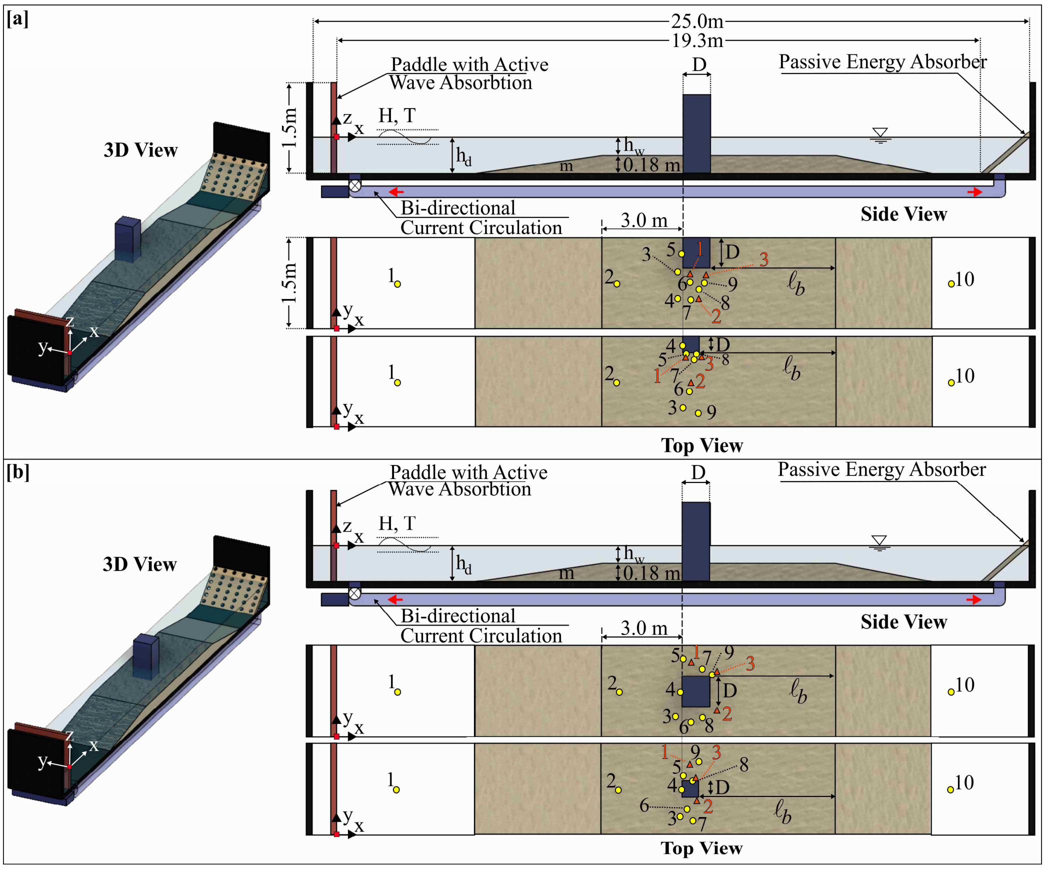

Figure 1: Schematic of experimental setup including WGs and ADVs locations. Panels (a) and (b) show two different layouts with structure on side, and at center of flume, respectively. Yellow circles and red rectangles represent WGs and ADVs, respectively.

Table 2: Coordinates of WGs and ADVs for different test cases

Instrument	Side				Center			
	D=0.50 m		*D=0.25 m*		*D=0.50 m*		*D=0.25 m*	
	x [m]	y [m]	x [m]	y [m]	x [m]	y [m]	x [m]	y [m]
WG1	-4.800	0.750	-4.800	0.750	-4.800	0.750	-4.800	0.750
WG2	-1.850	0.750	-1.850	0.750	-1.850	0.750	-1.850	0.750
WG3	-0.100	0.950	-0.010	1.365	-0.110	0.340	-0.040	0.305
WG4	-0.100	0.500	-0.010	0.330	-0.020	0.750	-0.010	0.750
WG5	-0.020	1.250	0.050	1.230	0.020	1.300	0.020	0.985
WG6	0.110	0.780	0.100	0.600	0.145	0.250	0.080	0.425
WG7	0.120	0.480	0.180	1.135	0.335	1.135	0.175	0.230
WG8	0.260	0.660	0.220	1.225	0.340	0.320	0.175	0.890
WG9	0.350	0.770	0.250	0.240	0.500	1.035	0.280	1.220
WG10	3.680	0.750	3.680	0.750	3.680	0.750	3.680	0.750
ADV1	0.110	0.920	0.040	1.175	0.150	1.250	0.125	1.180
ADV2	0.260	0.510	0.125	0.750	0.580	0.445	0.240	0.570
ADV3	0.380	0.900	0.300	1.180	0.580	1.100	0.225	0.950

2.2.2.Bathymetry measurement

A HR-Wallingford's HRBP-1070 bed profiler, operating in a three-dimension setting, was used to scan the berm surface before and after each test. The profiler's laser probe had an accuracy of ±0.5 mm and could function in both air and water. Before each test, the surface of the berm was leveled at 0.18 m above the flume bottom, then the water level was gradually increased to the target level. Subsequently, the profiler was calibrated to eliminate potential reading error due to ambient temperature variations and other factors. The scanned area included a total length of $5D$, $2D$ upstream, and $2D$ downstream of the structure. A blind zone of ~2 cm wide around the structure could not be fully scanned due to the maneuvering restrictions imposed by the probe arm assembly. Consequently, the bed elevation in that zone was manually measured.

2.3.Test Cases

To make it easier to refer to a particular test case, a naming convention is adopted here. This naming convention reflects the important specifications of each test—a letter S or C referring to the layouts, Side or Center, respectively, followed by the structure dimension in centimeters, and a dash followed by the wave height in centimeters. The specifications of the experimental setup for all test cases are summarized in Table 3.

Table 3: Specifications of all test cases

Test Case	h_d [m]	h_w [m]	H [m]	L [m]	D [m]	l_b [m]	m [m]	U_m [m/s]	KC [-]
S50-10	0.480	0.300	0.100	7.63	0.50	2.20	1:15	0.491	3.14
S50-7.5	0.405	0.225	0.075	6.83	0.50	2.20	1:15	0.406	2.55
S50-5.0	0.330	0.150	0.050	6.15	0.50	2.20	1:15	0.294	1.87
C50-10	0.480	0.300	0.100	7.63	0.50	2.20	1:15	0.491	3.14
C50-7.5	0.405	0.225	0.075	6.83	0.50	2.20	1:15	0.406	2.55
C50-5.0	0.330	0.150	0.050	6.15	0.50	2.20	1:15	0.294	1.87
S25-10	0.480	0.300	0.100	7.63	0.25	2.45	1:15	0.491	6.28
S25-7.5	0.405	0.225	0.075	6.83	0.25	2.45	1:15	0.406	5.11
S25-5.0	0.330	0.150	0.050	6.15	0.25	2.45	1:15	0.294	3.75
C25-10	0.480	0.300	0.100	7.63	0.25	2.45	1:15	0.491	6.28
C25-7.5	0.405	0.225	0.075	6.83	0.25	2.45	1:15	0.406	5.11
C25-5.0	0.330	0.150	0.050	6.15	0.25	2.45	1:15	0.294	3.75

In Table 3, h_w is the still water depth on the berm, l_b is the berm length from the leeside of the structure, and m is the slope of beaches on either side of the berm.

2.4.Experimental Procedure

In each test the following experimental procedure was followed:

i. Prior to each test, the surface of the berm was leveled, the water level in the flume was gradually increased to the target level, and an area of $3D \times 5D$ around the structure was scanned using the bed profiler.
ii. Wave gauges and ADVs were calibrated and positioned in their pre-designated positions.
iii. The solitary waves were generated by providing the wavemaker with the solitary wave time series.
iv. The flow field, i.e., the free surface elevations and 3D velocity fields, were recorded.
v. After the fluctuations in the flume were settled, the same area ($3D \times 5D$) was scanned.
vi. The bed elevation variation was calculated by subtracting the post and pre test bed elevations.

3.NUMERICAL MODEL: SedWaveFoam

The SedWaveFoam model (Kim et al., 2018), constructed using the open-source CFD toolbox, is an extension of the Eulerian two-phase model for sediment transport, SedFoam (Chauchat et al., 2017), by further merging the InterFoam (Berberović et al., 2009) which resolve free-surface wave propagations and waves2Foam (Jacobsen et al., 2012) which handles wave generation and absorption boundary conditions.

The SedWaveFoam model solves the Reynolds-averaged mass conservation equations for air, water, and sediment phases (Berberović et al., 2009; Drew, 1983). The governing equations are

$$\frac{\partial \phi^a}{\partial t} + \frac{\partial \phi^a u_i^a}{\partial x_i} = 0 \tag{1}$$

$$\frac{\partial \phi^w}{\partial t} + \frac{\partial \phi^w u_i^w}{\partial x_i} = 0 \tag{2}$$

$$\frac{\partial \phi^s}{\partial t} + \frac{\partial \phi^s u_i^s}{\partial x_i} = 0 \tag{3}$$

where the variables ϕ^a; ϕ^w and ϕ^s represent the volumetric concentration and u^a; u^w and u^s are the velocities of air, water, and sediment phases, respectively. The global mass conservation imposes $\phi^a + \phi^w + \phi^s = 1$.

The air and water phases are modeled as two immiscible fluids and their interface is resolved numerically by an interface tracking scheme (Berberović et al., 2009). The sediment phase, however, is modeled as a miscible phase in the fluids. Therefore, the mass conservation for the air and water phases is combined as the fluid phase, written as

$$\frac{\partial \phi^f}{\partial t} + \frac{\partial \phi^f u_i^f}{\partial x_i} = 0 \tag{4}$$

where the mixture of air and water phases is represented by superscript "f" with $\phi^a + \phi^w = \phi^f$ and $u^f = (\phi^a u^a + \phi^w u^w)/\phi^f$.

The use of air-water mixture as fluid phase results in simplification of three phases to two miscible phases which are air-water mixture (fluid) and sediment (solid) phases. Then, the simplified Reynolds-averaged momentum equations for fluid phase and sediment phase are given as

$$\frac{\partial \rho^f \phi^f u_i^f}{\partial t} + \frac{\partial \rho^f \phi^f u_i^f u_j^f}{\partial x_j} = -\phi^f \frac{\partial P^f}{\partial x_i} + \rho^f \phi^f g \delta_{i3} - \sigma_t \gamma_s \frac{\partial \phi^a}{\partial x_i} + \frac{\partial \tau_{ij}^f}{\partial x_j} + M_i^{fs} \tag{5}$$

$$\frac{\partial \rho^s \phi^s u_i^s}{\partial t} + \frac{\partial \rho^s \phi^s u_i^s u_j^s}{\partial x_j} = -\phi^s \frac{\partial P^f}{\partial x_i} - \frac{\partial P^s}{\partial x_i} + \rho^s \phi^s g \delta_{i3} - \sigma_t \gamma_s \frac{\partial \phi^s}{\partial x_i} + \frac{\partial \tau_{ij}^s}{\partial x_j} + M_i^{sf} \quad (6)$$

where ρ^s and ρ^f are the densities of sediment and air-water mixture with fluid density calculated as $\rho^f = (\phi^a \rho_{air} + \phi^w \rho)/\phi^f$. The terms P^f and P^s are the fluid and the particle pressures, respectively. The surface tension is defined as the multiplication of the surface tension coefficient, σ_t, and the surface curvature, γ_s. The terms τ_{ij}^f and τ_{ij}^s are fluid stress and particle shear stress, respectively. M^{fs} and M^{sf} represent inter-phase momentum transfer between fluid - sediment and sediment - fluid phases, which follows Newton's third law, i.e., $M^{fs} = M^{sf}$. M_i^{fs} is calculated by drag due to Reynolds-averaged velocity difference between the fluid and sediment phase and sediment flux due to turbulence.

$$M_i^{fs} = -\phi^s \beta \left(u_i^f - u_i^s\right) + \beta \frac{\upsilon^{ft}}{\sigma_c} \frac{\partial \phi^s}{\partial x_i} \quad (7)$$

where β, υ^{ft} and σ_c represent the drag parameter (Ding and Gidaspow, 1990), fluid turbulent viscosity, and Schmidt number, respectively. The turbulent eddy viscosity, υ^{ft}, is calculated by turbulent kinetic energy (TKE), k^f, and turbulent dissipation rate ε^f as $\upsilon^{ft} = C_\mu (k^f)^2/\varepsilon^f$ where C_μ is an empirical coefficient (Table 4).

The fluid stress, τ_{ij}^f (Eq.5), is composed of turbulent Reynolds stress (R_{ij}^{ft}) which represents the effect of turbulent fluctuations larger than grain scale and grain-scale components (r_{ij}^f) representing the small-scale viscous stress.

$$\tau_{ij}^f = R_{ij}^{ft} + r_{ij}^f = \rho^f \sigma^f \left[2\left(\upsilon^{ft} + \upsilon^f\right) S_{ij}^{ft} - \frac{2}{3} k^f \delta_{ij}\right] \quad (8)$$

where υ^f is the kinematic viscosity of fluid and calculated as

$$\upsilon^f = (\rho_{air} \phi^a \upsilon^a + \rho \phi^w \upsilon^w)/(\rho_{air} \phi^a + \rho \phi^w) \quad (9)$$

The terms υ^a and υ^w are the kinematic viscosity of air and water, respectively. S_{ij}^{ft} is the deviatoric part of the fluid phase strain rate and it is defined as

$$S_{ij}^{ft} = \frac{1}{2}\left(\frac{\partial u_i^f}{\partial x_j} + \frac{\partial u_j^f}{\partial x_i}\right) - \frac{1}{3}\frac{\partial u_k^f}{\partial x_k}\delta_{ij} \tag{10}$$

To model fluid turbulent viscosity, the standard balance equations of turbulent kinetic energy (TKE) and its dissipation rate are modified for two-phase flow, and they are written as

$$\frac{\partial \rho^f k^f}{\partial t} + \frac{\partial \rho^f k^f u_j^f}{\partial x_j} = R_{ij}^{ft}\frac{\partial u_i^f}{\partial x_j} + \frac{\partial}{\partial x_j}\left[\rho^f\left(\upsilon^f + \frac{\upsilon^{ft}}{\sigma_k}\right)\frac{\partial k^f}{\partial x_j}\right] - \rho^f\varepsilon^f - \frac{2\beta(1-\alpha_B)\phi^s k^f}{\phi^f} - \frac{\rho^f \upsilon^{ft}}{\phi^f \sigma_c}\frac{\partial \phi^s}{\partial x_j}(s-1)g\delta_{j3} \tag{11}$$

$$\frac{\partial \rho^f \varepsilon^f}{\partial t} + \frac{\partial \rho^f \varepsilon^f u_j^f}{\partial x_j} = C_{1\varepsilon}R_{ij}^{ft}\frac{\varepsilon^f}{k^f}\frac{\partial u_i^f}{\partial x_j} + \frac{\partial}{\partial x_j}\left[\rho^f\left(\upsilon^f + \frac{\upsilon^{ft}}{\sigma_\varepsilon}\right)\frac{\partial \varepsilon^f}{\partial x_j}\right] - C_{2\varepsilon}\rho^f\frac{\varepsilon^f}{k^f} - C_{3\varepsilon}\frac{\varepsilon^f 2\beta(1-\alpha)\phi^s k^f}{k^f\,\phi^f} - C_{4\varepsilon}\frac{\varepsilon^f \rho^f \upsilon^{ft}}{k^f \phi^f \sigma_c}\frac{\partial \phi^s}{\partial x_j}(s-1)g\delta_{j3} \tag{12}$$

where σ_c= 1 is the empirical TKE Schmidt number (e.g., Rodi, (1993)) and s is the specific gravity of the sediment. The last two terms on the right-hand side of Eq. (11) and Eq. (12) represent the effect of sediment on modifying carrier flow turbulence (Chauchat et al., 2017). $C_{1\varepsilon}$, $C_{2\varepsilon}$, $C_{3\varepsilon}$, $C_{4\varepsilon}$, and σ_ε are the empirical coefficients summarized in Table 4.

Table 4: List of Model Coefficients for Fluid Turbulence Closure

C_μ	$C_{1\varepsilon}$	$C_{2\varepsilon}$	$C_{3\varepsilon}$	$C_{4\varepsilon}$	σ_c	σ_ε
0.09	1.44	1.92	1.2	1.0	1.0	1.3

The particle pressure, P^s, and particle shear stress, τ_{ij}^s, are expressed as the summation of a collisional component and a frictional contact component caused by intergranular interactions (Hsu and Hanes, 2004). The superscripts "sc" and "sf" in Eq. (13) and Eq. (14) corresponds to a collisional component and a frictional contact component, respectively.

$$P^s = P^{sc} + P^{sf} \tag{13}$$

$$\tau_{ij}^{s} = \tau_{ij}^{sc} + \tau_{ij}^{sf} \tag{14}$$

The concept of granular temperature, Θ, in the kinetic theory of granular flow (Ding and Gidaspow, 1990; Jenkins and Savage, 1983) is used to model the collisional component of particle pressure, P^{sc}, and particle shear stress, τ_{ij}^{sc}. The reader is kindly referred to Chauchat et al. (2017) for more details.

The particle pressure due to enduring contact, P^{sf}, is calculated as

$$P^{sf} = \begin{cases} 0 & \phi^s < \phi_f^s \\ 0.05 \dfrac{\left(\phi^s - \phi_f^s\right)^3}{(\phi_{max}^s - \phi^s)^5} & \phi^s \geq \phi_f^s \end{cases} \tag{15}$$

To model the solid-like behavior of sediment bed in high concentration, the frictional viscosity, μ^{sf}, is calculated as

$$\mu^{sf} = \frac{\sqrt{2} P^{sf} \sin\theta_s}{2\sqrt{S_{ij}^{s} S_{ij}^{s}}} \tag{16}$$

where θ_s is the angle of repose, taken to be 28° for sand. Then, the particle shear stress due to enduring contact, τ_{ij}^{sf}, is calculated as

$$\tau_{ij}^{sf} = -2\mu^{sf} S_{ij}^{s} \tag{17}$$

4.RESULTS

Changes in the bathymetry at the end of each test as well as the skill of the SedWaveFoam model in simulating the flow field and bed evolution for Case S50-10 are presented and discussed in the following subsections.

4.1.Experiments

Figure 2 shows the plan view of the normalized final bathymetric change (S/D) for all test cases. The cold color represents the scour ($S/D < 0$) and the hot color shows the sediment deposition ($S/D > 0$). The scour holes appear in the vicinity of the sharp edges, both on the seaside and leeside of the structure. It is evident that the scour footprint is larger on the leeside of the structure. The scour holes, whose depths vary between $0.017D$ to $0.044D$, appear to be stretched and oriented at ~45° with respect to the incident wave direction. The traces of sediment deposits, with a thickness ranging between $0.037D$ and $0.07D$, appear near the scour holes as well as along the green spiral curves marked in Figure 2. These spiral curves show the trajectories of the migrating wake vortices originated at the sharp edges. These energetic vortices are believed to be the primary driving mechanism of the scouring, entraining, and entrapping the sediment particles, keeping them in suspension, carrying them along, and releasing them while propagating along the spiral trajectories. For the cases with the smallest wave height (i.e., $H = 0.05$m), however, the wake vortex dissipates rapidly before being able to transport the suspended sediment away from the structure—contrary to those of the cases with the larger waves (i.e., H= 0.1m and 0.075m) in which the suspended sediment is transported to a distance of $\sim D$ away from the structure. .

Figure 3 shows the scour footprint dimension, defined as the arithmetic mean of the width of the scoured area in x and y directions, R_a, for each test case. The average width and maximum depth of the scour holes are summarized in Table 4. The results indicate that the largest scour depths, ranging between $0.028D$ and $0.044D$, are associated with the test cases in which both wave height and water level are the greatest. (i.e., S50-10, C50-10, S25-10 & C25-10). Also, the scour depth and width increase with the structure dimension. More importantly, a measurable variation of the scour characteristics, both width and depth, can be spotted between the two layouts. The side layout leads to a greater scour than the center layout. It is also worth mentioning that in all cases, the scour depth on the seaside is greater than that of the leeside. On the contrary, the width of the scour hole is larger on the leeside than the seaside. For the center layout, a symmetric scour pattern near the corners of the structure can be observed. This pattern is the signature of the symmetric vortices generated near the corners of the structure, following the impingement of the solitary waves on the sharp-edged structure (Sogut et al., 2019).

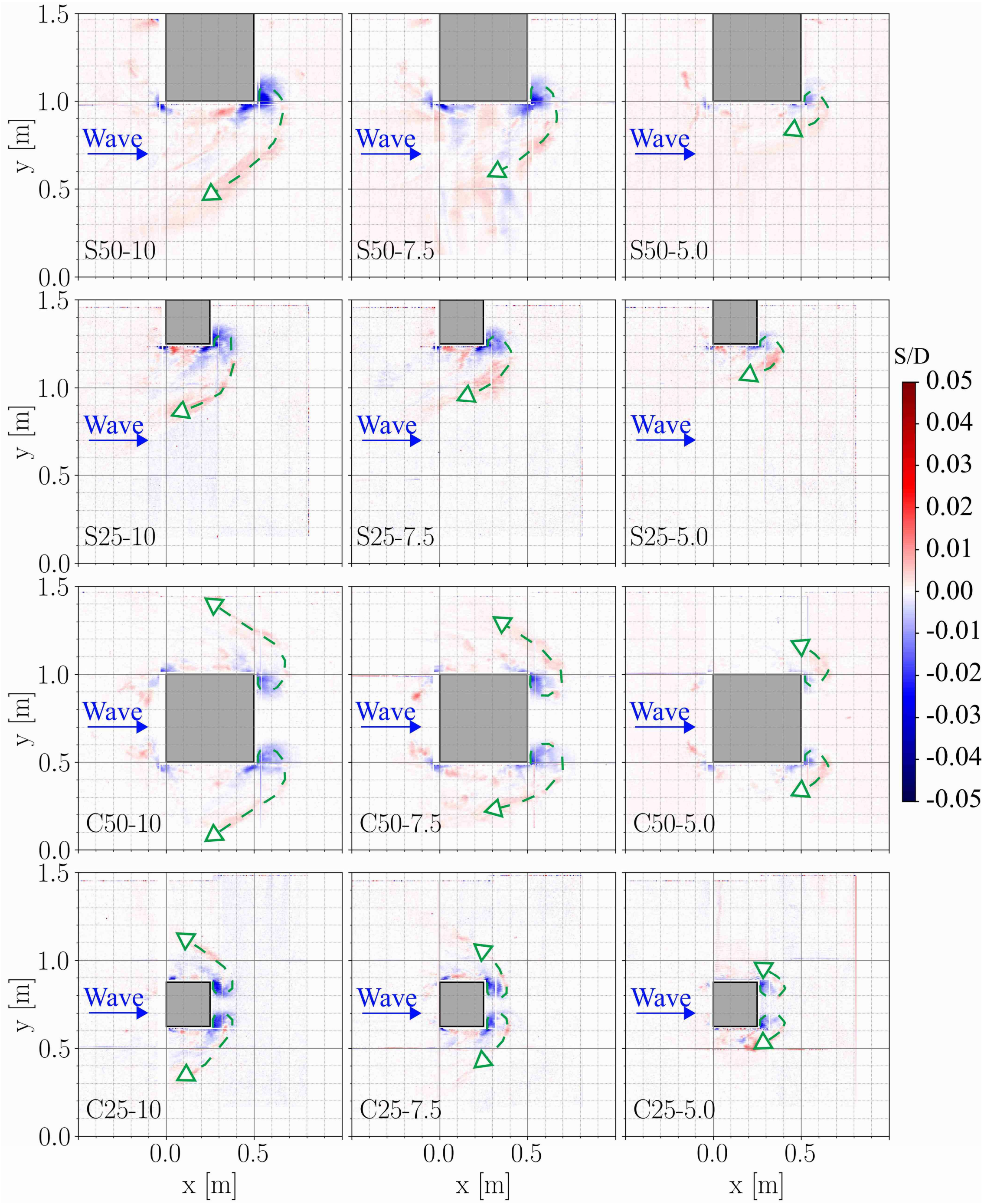

Figure 2: Plan view of normalized bathymetry change as well as trajectories of vortices, for each test case. Gray square represents the structure

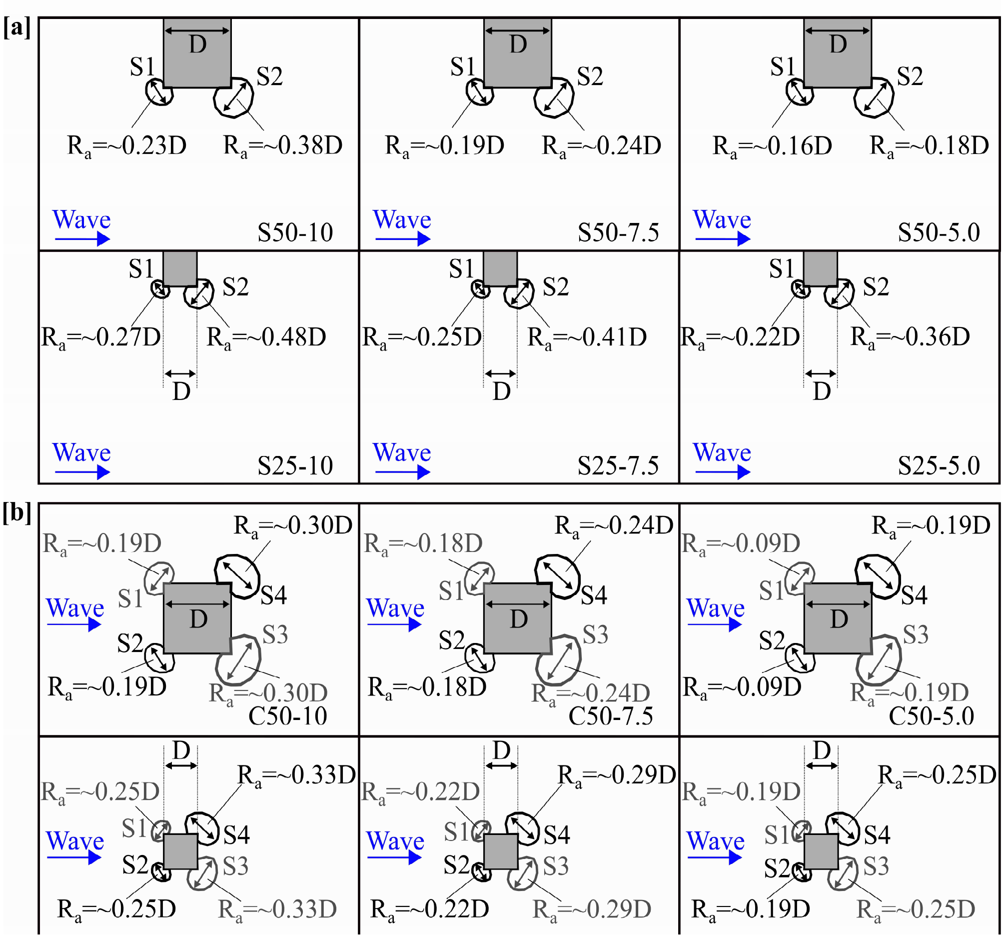

Figure 3: Plan view of scour footprints (width) and their dimensions: [a] side layout, and [b] center layout

Table 5: Specifications of scour depth and width for all test cases

Test Case	Seaside		Leeside		$\lvert\text{Seaside} - \text{Leeside}\rvert/\text{Leeside}$	
	S/D [-]	R_a/D [-]	S/D [-]	R_a/D [-]	S/D [%]	R_a/D [%]
S50-10	0.033	0.225	0.032	0.375	3.1	40.0
S50-7.5	0.030	0.190	0.029	0.240	3.4	20.8
S50-5.0	0.017	0.155	0.015	0.180	13.3	13.9
S25-10	0.044	0.270	0.042	0.480	4.8	43.8
S25-7.5	0.034	0.250	0.032	0.410	6.3	39.0
S25-5.0	0.032	0.220	0.031	0.360	3.2	38.9
C50-10	0.028	0.185	0.023	0.298	21.7	37.9
C50-7.5	0.021	0.175	0.020	0.240	5.0	27.1
C50-5.0	0.018	0.088	0.017	0.188	5.9	53.2
C25-10	0.035	0.250	0.030	0.330	16.7	24.2
C25-7.5	0.031	0.220	0.028	0.285	10.7	22.8
C25-5.0	0.028	0.185	0.025	0.250	12.0	26.0

4.2. Numerical Model: Validation

Case S50-10 is selected to evaluate the SedWaveFoam model performance as it entailed the most energetic flow condition with the highest shielding effect.

The sensitivity of the model to the mesh size in simulating the flow field and bed evolution is assessed using (i) nested, and (ii) hybrid meshes as illustrated in Figure 4. In the nested mesh, the mesh size around the structure is locally refined, with the finest mesh size of 0.5cm in all directions. On the other hand, the mesh in the hybrid mesh is gradually refined from the numerical wave flume (NWF) boundaries towards the structure as well as towards the surface of the erodible bed. In this mesh alternative the finest mesh sizes are 0.45m in the x and y directions, and 0.15m in the z direction. The total numbers of grid points in the nested and hybrid mesh settings are 6.4×10^6 and 9.8×10^6, respectively. The clock time required to complete a 15-second simulation for Case S50-10 is ~67 h for the nested mesh, and ~176 h for the hybrid mesh on a cluster of five Intel Xeon E5-2670 nodes, each with 16 cores (i.e., 80 cores, in total).

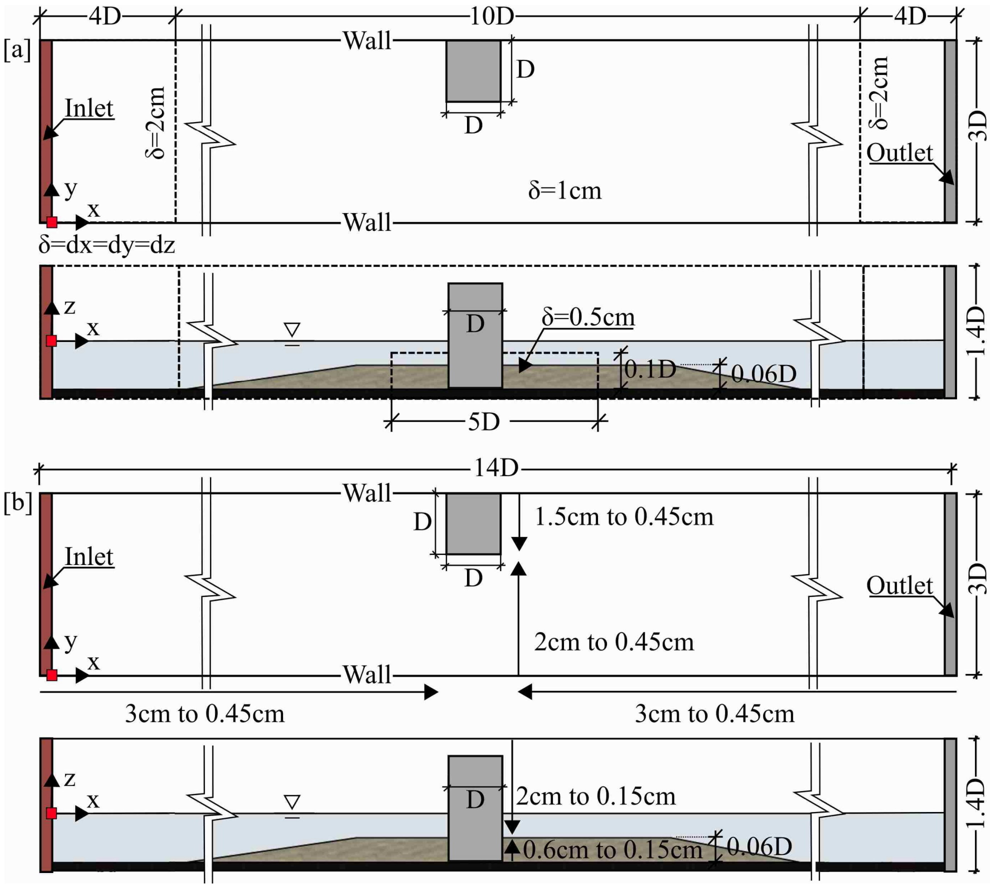

Figure 4: Plan and side views of numerical wave flume showing mesh sizes for [a] nested and [b] hybrid mesh alternatives. Figure not to scale. *dx, dy* and *dz* are grid sizes in *x, y* and *z* directions, respectively.

Figure 5 illustrates the comparisons of the measured and simulated free surface elevations (η) at various wave gauge positions and time instants. The performance of the SedWaveFoam model is quantified using the Normalized Root Mean Square Error (NRMSE) metric (Table 6). Overall, the SedWaveFoam model is found to be relatively insensitive to the mesh size in simulating the free surface elevations along the NWF.

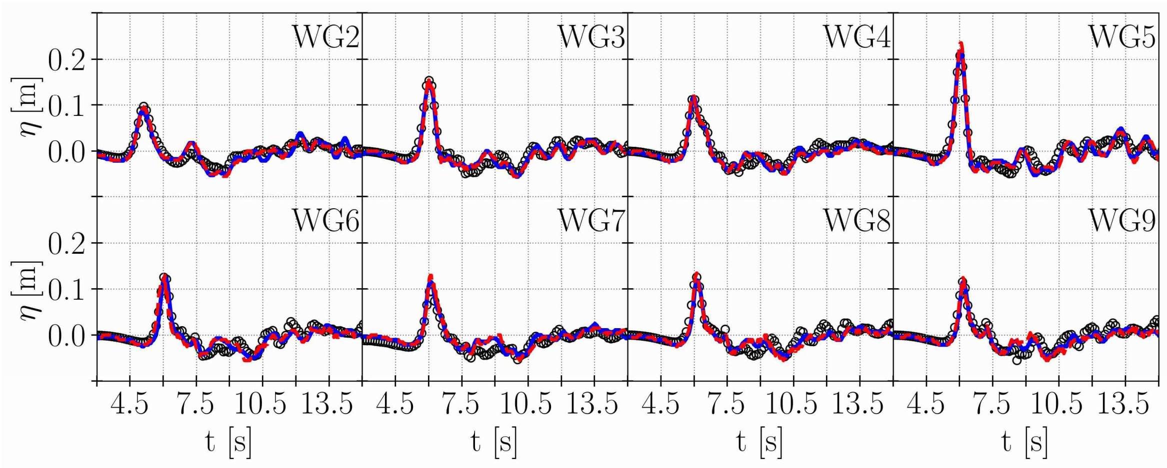

Figure 5: Comparisons of measured and simulated free surface elevations (η) at various wave gauges. Black circles represent measured η. Blue solid and red dashed lines indicate the modeled η for nested and hybrid mesh settings, respectively.

Table 6: SedWaveFoam model performance metric for free surface elevation.

	Mesh Alternative	WG 2	3	4	5	6	7	8	9
NRMSE [%]	nested	3.4	3.1	3.2	2.6	2.9	3.7	3.3	3.2
	hybrid	2.6	2.2	2.4	2.3	3.1	3.7	3.3	3.3

The noise originated from the air entrainment and sediment suspension is removed from the measured velocity data by applying a band-pass filter that takes into account the correlation (≥70%) and Signal-to-Noise Ratio (SNR) (≥10-15) criteria regarding the reliable velocity signals. Figure 6 depicts the temporal variations of the streamwise (u), spanwise (v), and vertical (w) velocity components, at ADV1, ADV2, and ADV3. Table 7 summarizes the model performance metrics for replicating the velocity field. The NRMSE values, ranging between 12.1% – 21.1%, indicate that the SedWaveFoam model performs well in predicting the velocity field. The computed streamwise and vertical velocity components show the most and the least agreements with the measured data, respectively. The residual noise may be responsible for some of the discrepancies between the simulated and measured velocities.

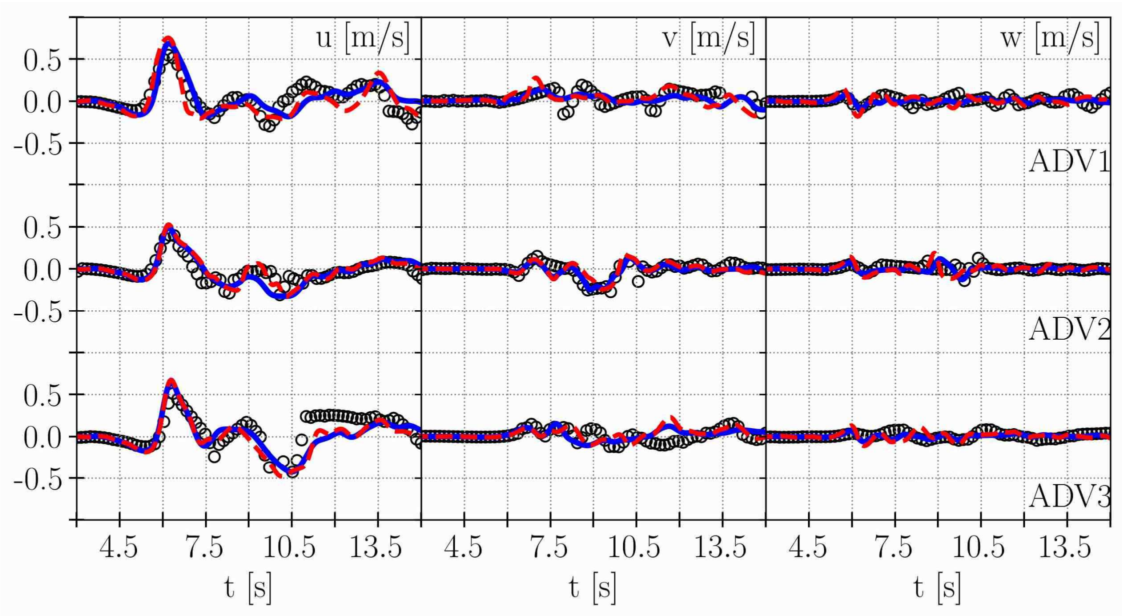

Figure 6: Comparisons of normalized filtered-measured and simulated streamwise (u), spanwise (v), and vertical (w) velocities. Black circles represent measured velocity components. Blue solid and red dashed lines indicate the modeled velocity components for nested and hybrid mesh settings, respectively.

Table 7: SedWaveFoam model performance metric for velocity field

		ADV1			ADV2			ADV3		
	Mesh setting	u	v	w	u	v	w	u	v	w
NRMSE [%]	nested	15.3	16.4	20.7	12.1	19.9	14.7	20.8	13.0	16.7
	hybrid	15.6	17.2	20.9	10.9	21.1	18.9	20.3	15.5	20.6

Figure 7 compares the measured and modeled bathymetric changes based on the two mesh settings. Although the SedWaveFoam model appears to be only slightly sensitive to the mesh size in resolving the flow hydrodynamics, the bathymetric changes are highly sensitive to the mesh size—mesh refinement in the hybrid setting considerably improves the predicted bathymetry. Thus, the analysis is proceeded based on the results of the hybrid mesh setting. The mesh refinement significantly improves the predictions of the leeside scour; however, the leeside scour is underpredicted. This discrepancy is probably associated with the use of the $k - \varepsilon$ model which inherently underpredicts the intensity of the vortex in the case of the adverse pressure (Menter and Esch, 2001; Menter et al., 2003; Pope, 2001; Wilcox, 1998) induced due to the flow blockage.

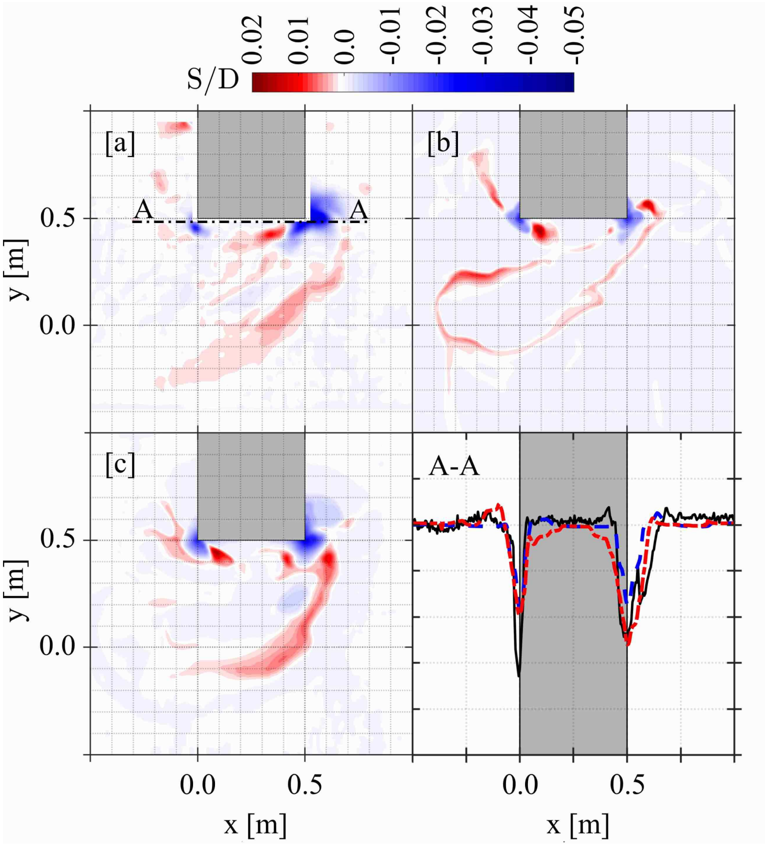

Figure 7: Plan views of [a] measured and [b-c] simulated bed elevation variation. Panels [b], and [c] indicate nested and hybrid mesh alternatives, respectively. Right bottom panel is cross-sectional view of measured and simulated bed elevation variations along A-A line shown in [a]. Black solid line represents measured bed elevation variation. Blue and red dashed lines indicate simulated bed elevation variations for nested and hybrid mesh alternatives, respectively.

5.DISCUSSIONS

In the following, the scour characteristics are synthesized in detail followed by the sensitivity analysis of the scour with respect to the flow characteristics, i.e., wave height, and water level.

5.1.Blockage Effect on Near-bed Velocity

Although the flow blockage is typically disregarded when studying the scour around a slender cylinder in the laboratory, such an assumption may not be acceptable for non-slender structures as the blockage could potentially modify the flow (e.g., Goseberg and Schlurmann (2012, 2011)). Consequently, the scouring processes could be affected by the flow blockage. To address this issue, the undisturbed near-bed velocity, U_m, was measured—in the absence of the structure—at a single location where, later, ADV1 (Figure 1-[b]) and ADV2 (Figure 1-[a]) were positioned. In order to account for the blockage effects on the scouring process on the leeside of the structure where the blockage resulted in a flow velocity gradient and, in turn, the formation of stronger eddies (Sogut et al., 2020, 2019), the velocity is first adjusted before being used to develop the quantitative description of the scour patterns, following Sogut and Farhadzadeh (2020). The blockage ratio, B_R, is defined as the ratio of the projected width of the structure, perpendicular to the incident wave, to the width of flume. Subsequently, a relationship is developed linking the blockage ratio and the maximum undisturbed flow velocity, U_{ub}, measured at an elevation of one-third the still water depth above the berm, to the maximum disturbed flow velocity, U_b, measured at the same depth in the presence of the structure. The velocities, U_{ub} and U_b, were measured at the representative locations as shown in Figure 8 - [a]. The resulting relationship, based on the measured data for all test cases, is presented by Eq. (18). Figure 8 - [b] shows the comparison of the measured and predicted U_b.

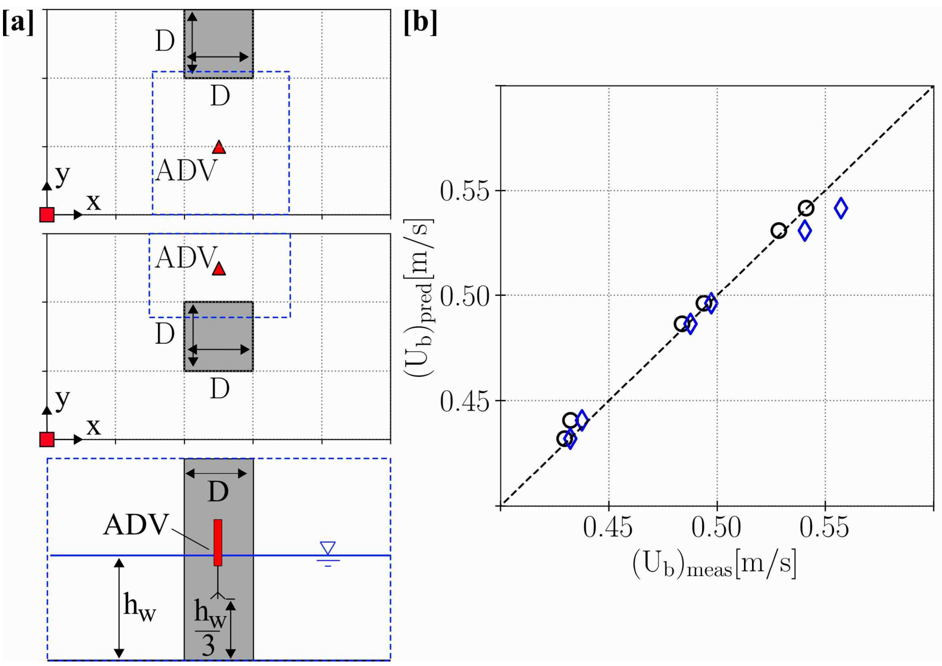

Figure 8: [a] Position of ADV used for assessing blockage effect on flow velocity; [b] Comparison of predicted $(U_b)_{pred}$ and measured $(U_b)_{meas}$velocities for all test cases. Black circle and blue diamond represent side and center layouts, respectively

$$\frac{U_b}{U_{ub}} = 0.1224(B_R) + 1.00 \tag{18}$$

Eq. (18)is valid for $0.167 \leq B_R \leq 0.33$, the range of the blockage in the present experiment.

Assuming that the near-bed velocity follows the same trend as U_b, the disturbed near-bed velocity (U_{mm}) is calculated by adjusting the measured undisturbed near-bed velocity (U_m) according to Eq. (18). It should be noted that this adjustment is applied only to the analysis of the scour on the leeside where the blockage is thought to modify the velocity more significantly. For the assessment of the scour on the seaside, the measured near-bed velocity, U_m, is used without further adjustments. The measured and modified near-bed velocity data, as well as the calculated KC values, are summarized in Table 8. The table shows that the streamwise velocity increases by ~4% when the blockage is the highest (i.e., $B_R = 0.33$). For the smaller structure with $B_R = 0.167$, the velocity increases ~2%.

Table 8: Near-bed velocities and corresponding KC

D [m]	h_w [m]	H [m]	T [s]	B_R [-]	Seaside		Leeside		$\lvert U_{mm} - U_m \rvert / U_m$ [%]
					U_m [m/s]	KC [-]	U_{mm} [m/s]	KC [-]	
0.50m	0.300	0.100	3.20	1/3	0.491	3.14	0.511	3.28	4.1
	0.225	0.075	3.15	1/3	0.406	2.55	0.422	2.66	4.1
	0.150	0.050	3.19	1/3	0.294	1.87	0.306	1.96	4.1
0.25m	0.300	0.100	3.20	1/6	0.491	6.28	0.501	6.41	2.0
	0.225	0.075	3.15	1/6	0.406	5.11	0.414	5.21	2.0
	0.150	0.050	3.19	1/6	0.294	3.75	0.300	3.82	2.0

5.2. Flow Regime in Solitary Wave Boundary Layer

The flow regime in a solitary wave boundary layer can be described by the Reynolds number (Re), similar to an oscillatory boundary layer (Sumer and Fuhrman, 2020). The Reynolds number of a solitary wave boundary layer is defined as

$$Re = \frac{aU_n}{\upsilon} \tag{19}$$

where U_n is the near-bed velocity (U_m or U_{mm}, here), υ is the kinematic viscosity of water, and a is the free stream amplitude, given by

$$a = \frac{U_n T}{2\pi} \tag{20}$$

with T being the wave period which is calculated as described in Section 2.1. Even though this relationship was proposed for a smooth bed, it is adopted here as an approximation to understand the flow regime in the boundary layer. However, further studies need to be conducted to accurately predict the flow regime in the solitary wave boundary layer for transitional/rough beds.

A Reynolds number greater than 2×10^5 indicates that the boundary layer transitions from laminar to turbulent (Carstensen et al., 2010; Fredsøe and Deigaard, 1992; Fuhrman et al., 2009a, 2009b; Sumer et al., 2010). The corresponding bed shear stress can be expressed as (Fredsøe, 1984; Fredsøe and Deigaard, 1992)

$$\tau = \frac{1}{2}\rho f_w {U_n}^2 \tag{21}$$

where f_w is the wave friction factor, and ρ is the density of water.

The friction factor for a hydraulically smooth surface is a function of the Reynolds number.

$$R_e^* = k_N U_{fm}/\upsilon \; < \; 5 \tag{22}$$

where U_{fm}, k_N and R_e^* are the maximum friction velocity, the Nikuradse roughness, and the roughness Reynolds number, respectively.

The friction factor is independent of the Reynolds number for a hydraulically rough (R_e^*> 70) or transitional regimes (5< R_e^*< 70), instead it is a function of the dimensionless parameter a/k_N (Carstensen et al., 2010; Fuhrman et al., 2009b, 2009a; Sumer et al., 2010; Sumer and Fuhrman, 2020). Here, the adopted Nikuradse roughness is $k_N = 2.5D_{50}$ (Soulsby, 1997; Sumer et al., 2007). The empirical wave friction coefficient may be expressed as (Fuhrman et al., 2013; Sumer and Fuhrman, 2020).

$$f_w = exp\,[5.5\,(\frac{a}{k_N})^{-0.16} - 6.7] \quad (23)$$

Table 9 summarizes the magnitudes of the Reynolds number (Re) and dimensionless bed shear stress ($\tau^* = \tau/\rho g h_w$). It becomes evident from Table 9 that for all test cases, the boundary layer on either side of the structure is laminar and the sandy berm is classified as a hydraulically transitional boundary. The normalized bed shear stress on the seaside ranges between 3.67×10^{-4} and 4.26×10^{-4}, and on the leeside varies between 3.71×10^{-4} and 4.58×10^{-4}. The relatively small enhancement of the bed shear stress on the leeside is because of the flow blockage, which is discussed in regard to the scour characteristics in the following.

Table 9: Summary of flow regime in solitary wave boundary layer for all test cases

Test Case	Seaside					Leeside				
	a/k_N [-]	R_e^* [-]	Re ($\times10^4$) [-]	f_w ($\times10^{-2}$) [-]	τ^* ($\times10^{-4}$) [-]	a/k_N [-]	R_e^* [-]	f_w ($\times10^{-2}$) [-]	Re ($\times10^4$) [-]	τ^* ($\times10^{-4}$) [-]
S50-10 C50-10	369.9	23.9	12.25	1.041	4.26	386.4	24.8	1.026	12.79	4.58
S25-10 C25-10	369.9	23.9	12.25	1.041	4.26	372.3	24.0	1.039	12.32	4.30
S50-7.5 C50-7.5	301.1	20.5	8.25	1.119	4.17	314.5	21.2	1.102	8.61	4.48
S25-7.5 C25-7.5	301.1	20.5	8.25	1.119	4.17	303.0	20.6	1.116	8.30	4.22
S50-5.0 C50-5.0	220.8	15.7	4.38	1.251	3.67	230.6	16.3	1.231	4.58	3.94
S25-5.0 C25-5.0	220.8	15.7	4.38	1.251	3.67	222.2	15.8	1.249	4.41	3.71

5.3. Scour Characteristics

Linking the equilibrium scour depth to the Keulegan–Carpenter number, and the Shields parameter have been attempted by several researchers in the past. Some of those studies are reviewed in this paper. In the following, the relationships between these important parameters and the characteristics of the solitary wave-induced non-equilibrium scour are examined.

5.3.1. Correlations between Keulegan–Carpenter number and scour characteristics

Figure 9 shows the variations of the dimensionless scour depth, S/D, and width, R_a/D, with respect to KC. The figure demonstrates that irrespective of the structure dimension or layout, S/D increases with KC more rapidly on the seaside than the leeside. On the other hand, R_a/D increases with KC more rapidly on the leeside than the seaside, owing to the formation of larger eddies associated with the greater KC which entails a higher bed shear stress on the leeside corner of the structure. The magnitudes of S/D and R_a/D vary relatively linearly with KC. Figure 9 also shows that the variation of the dimensionless scour volume, V_a/V_D, with respect to KC follows a power-law. Since the scour holes have a conical geometry, their volumes are calculated by setting S/D and R_a/D as the height and diameter of the cone, respectively. It is evident that a larger amount of sediment is removed from the leeside of the structure than the seaside—the scour hole volume is ~50% larger on the leeside. This may indicate that most of the sediments deposited near the structure, as shown in Figure 2, are supplied by the sediments entrained in the wake vortices following the formation of the leeside scour. The difference between the seaside and leeside scour volumes becomes much greater with the increase of KC.

Figure 10, another representation of the data shown in Figure 6, helps visualize how the scour depth, average width, and volume vary with KC for the two structure dimensions. Both parameters, S/D and R_a/D, increase with KC—subsequently the scour volumes on both sides of the structure increase with KC. For a given KC, the larger the structure, the deeper and wider the scour hole. This is because KC is inversely related to the structure dimension and maintaining the KC constant for the larger structure requires a stronger velocity. Subsequently, the stronger flow leads to the greater shear velocity and larger scour. Thus, the scour characteristics for the non-slender structure appear to be controlled by the structure dimension.

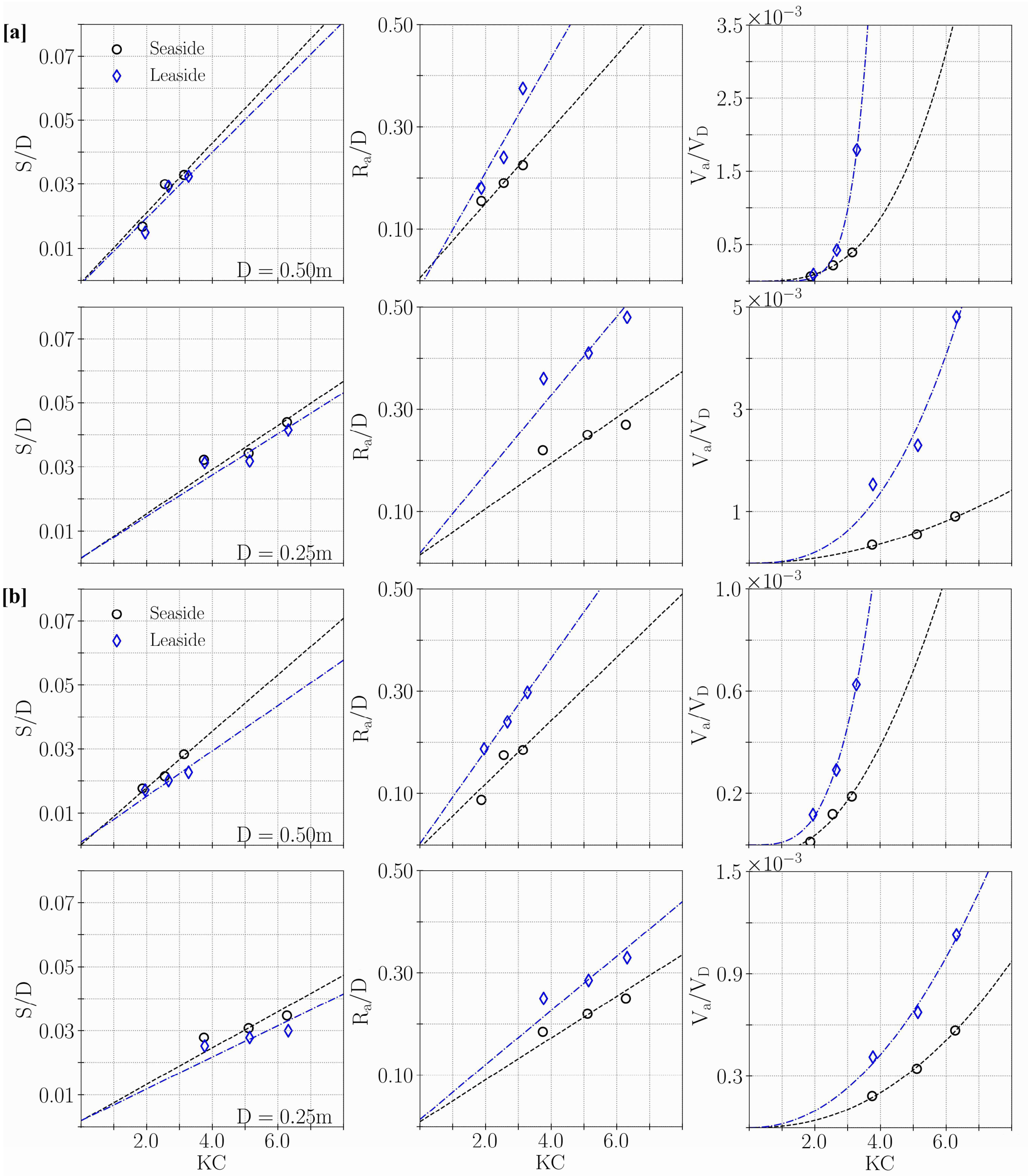

Figure 9: Variations of S/D, R_a/D and V_a/V_D with respect to KC for [a] side layout [b] center layout. Characteristic volume, V_D, is a product of cross-sectional area of structure and unit height.

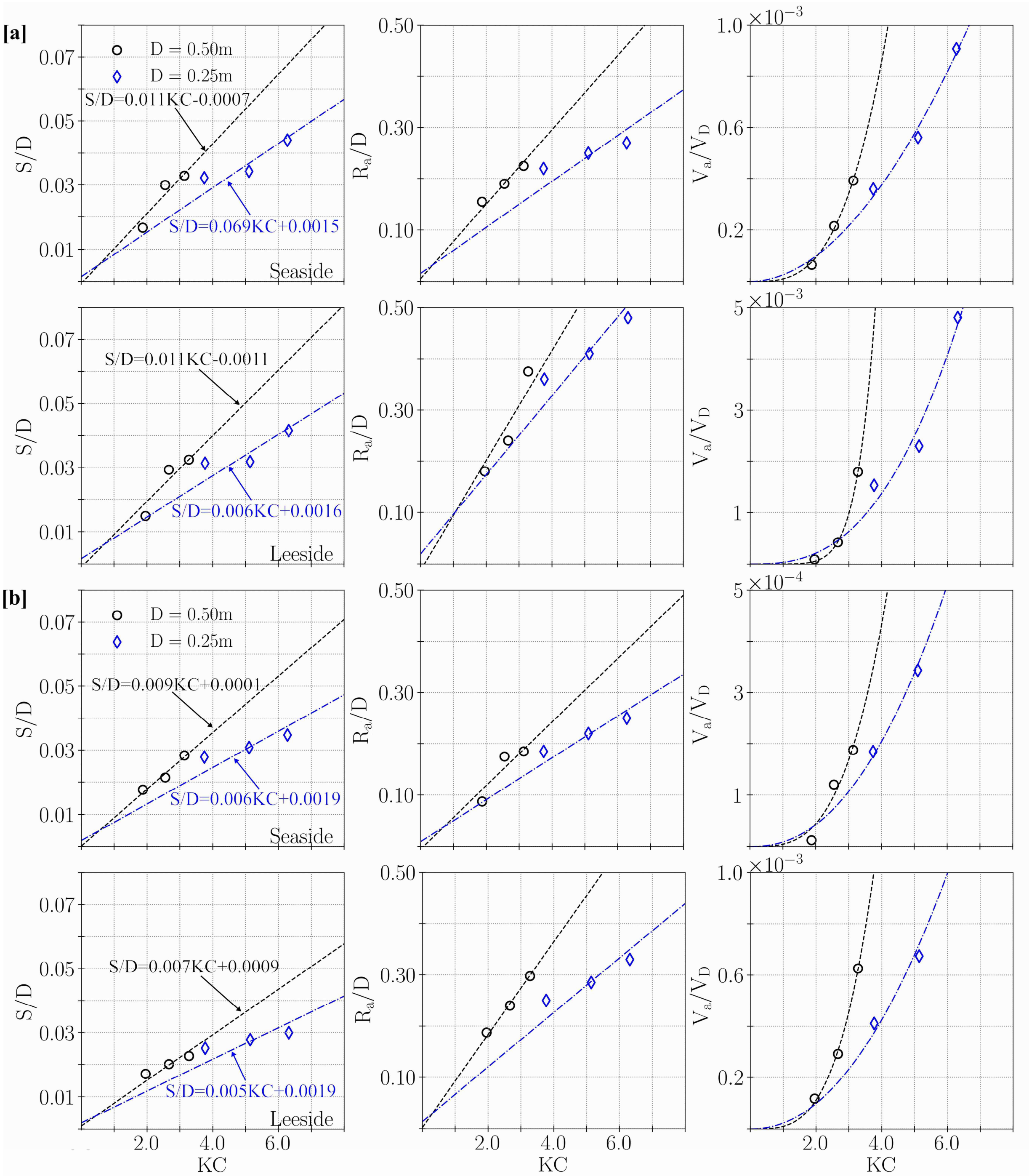

Figure 10: Variation of S/D, R_a/D and V_a/V_D with respect to KC for two structure dimensions and for [a] side layout [b] center layout. Characteristic volume, V_D, is a product of cross-sectional area of structure and unit height.

5.3.2. Correlations between Shields parameter and scour characteristics

In this study, the primary driving mechanism of scouring by the solitary wave is shown to be the wake vortices which entrap the suspended sediment particles at the sharp edges of the structure and carry them away. The dimensionless grain size (D_*) and the associated critical Shields parameter (θ_{cr}) are the two important factors often used to describe the particle suspension threshold (Soulsby, 1997; Soulsby and Whitehouse, 1997; Whitehouse, 1998). Whitehouse (1998) established relationships between D_* and θ_{cr} of cohesionless sediment under wave, current, and combined wave-current actions. The dimensionless grain size can be defined as

$$D_* = D_{50}\left[\frac{(s-1)g}{\upsilon}\right]^{1/3} \tag{24}$$

where g is the acceleration due to the gravity; and s is the sediment's specific gravity.

The Shields parameter (Sumer and Fredsøe, 2002; Sumer and Fuhrman, 2020) is stated as

$$\theta = \frac{{U_{fm}}^2}{(s-1)gD_{50}} \tag{25}$$

where U_{fm} represents the maximum value of the friction velocity which is defined as (Fredsøe, 1984; Sumer et al., 2007; Sumer and Fredsøe, 2002; Sumer and Fredsøe, 2001)

$$U_{fm} = \sqrt{0.5f_w}\,U_{mm} \tag{26}$$

Soulsby (1997) and Soulsby and Whitehouse (1997) suggested a critical Shields parameter, θ_{cr}, applicable to sediment particles with D_*<10.

$$\theta_{cr} = \frac{0.30}{1+1.2D_*} + 0.55[1 - exp(-0.02D_*)] \tag{27}$$

The parameter θ_{cr} is used to determine the initiation of the particle motion. To determine whether the sediment particles are entrapped and transported by wake vortices, the critical Shields parameter for the suspended sediment entrapment, θ_s, is employed (Sumer et al., 2007).

$$\theta_s = \left(\frac{U_{0fm}D_{50}}{\upsilon}\right)^{-0.05}\left[0.7exp\left(-0.04\frac{U_{0fm}D_{50}}{\upsilon}\right)\right] + 0.26\left[1 - exp\left(-0.025\frac{U_{0fm}D_{50}}{\upsilon}\right)\right] \quad (28)$$

where U_{0fm} is the maximum shear velocity at the edge of the structure, which can be linked to U_{mm} using (Sumer et al., 1997)

$$U_{0fm} = \sqrt{2f_w}\, U_{mm} \quad (29)$$

The criterion for sediment suspension, entrapment, and transport by a wake vortex leads to $\theta > \theta_s/4$ (Sumer et al., 2007). For the median grain diameter in the current study (i.e., D_{50}=0.27mm), the dimensionless grain size is $D_* = 6.83$, with $s = 1.65$ and $\upsilon = 10^{-6}\ \mathrm{m^2/s}$. Consequently, Eq.(27) yields the critical Shields parameter $\theta_{cr} \approx 0.04$.

Figure 11 depicts the variation of the scour depth on the leeside of the structure with respect to the Shields parameter. The sediment particles on the leeside which begin to move (θ/θ_{cr}>1) are suspended and entrapped by the wake vortex ($\theta > \theta_s/4$) in all test cases. Although, for a given Shields parameter, the scour depth increases with the structure dimension, the greater dimensionless scour depth (S/D) is associated with the smaller structure.

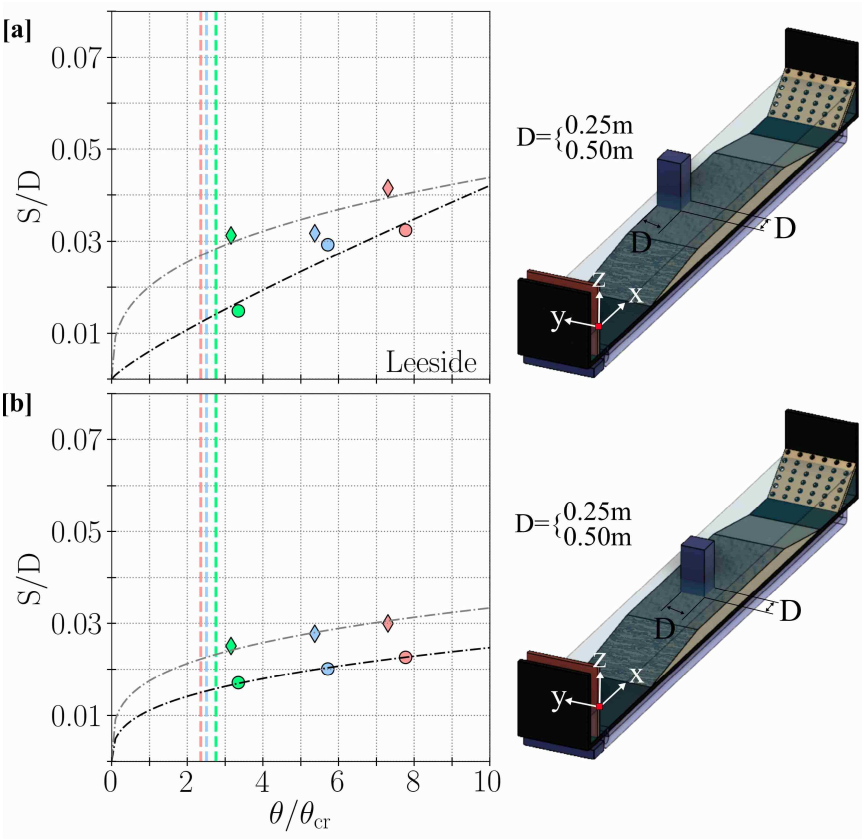

Figure 11: Variation of S/D on the leeside of structure with respect to θ/θ_{cr} for: [a] side layout; [b] center layout; circles and diamonds represent D=0.50m and D=0.25m, respectively; black and gray dashed-dot lines are fitted curves for D=0.50m and D=0.25m, respectively; dashed vertical lines represent critical Shields parameters for sediment suspension and entrapment by wake vortices ($\mathrm{i.e.}, \theta = \theta_s/4$), green, blue, and red colors correspond to wave heights 0.05, 0.075, and 0.10m, respectively.

5.4. Uncertainty Analysis

To quantify the uncertainties associated with the maximum non-equilibrium scour depth around the structure $(S/D)_{max}$, the Monte Carlo simulations are carried out. First, empirical relationships between $(S/D)_{max}$ and KC are developed by fitting curves to the presented data in the previous section. To generate KC for a broad range of waves and water levels, relationships are established for the maximum near-bed velocity, U_n, as a function of the wave celerity, c, wave height (H), and water depth (h_d), using the data measured for the twelve test cases (Figure 12). The wave period is calculated as described in Section 2.1.

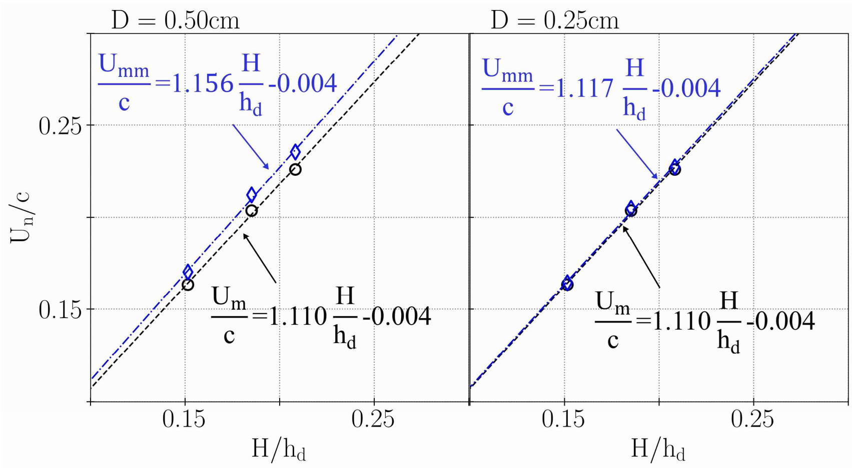

Figure 12: Maximum near-bed velocity (U_n) as a function of wave celerity (c), wave height (H) and water depth (h_d). Black circle and blue diamond represent seaside and leeside, respectively.

Subsequently, a large population of water depths and wave heights are randomly generated. The random wave heights and water levels range between H_{max}= 0.10 m and H_{min}= 0.05m, and $h_{w,max}$= 0.30 m and $h_{w,min}$= 0.15 m, respectively. These uniformly distributed data, which include a million combinations of wave height and water level, are used as input to the Monte Carlo model to produce the maximum normalized scour depths. The empirical relationships and the procedure for the Monte Carlo simulation are presented in the flowchart presented in Figure 13. The Monte Carlo simulation is carried out based on two different approaches, (1) to develop the maximum dimensionless scour depth relationship for each layout and structure dimension, separately, and (2) to establish a generic relationship for the maximum dimensionless scour depth that is applicable to various structure dimensions and layout settings.

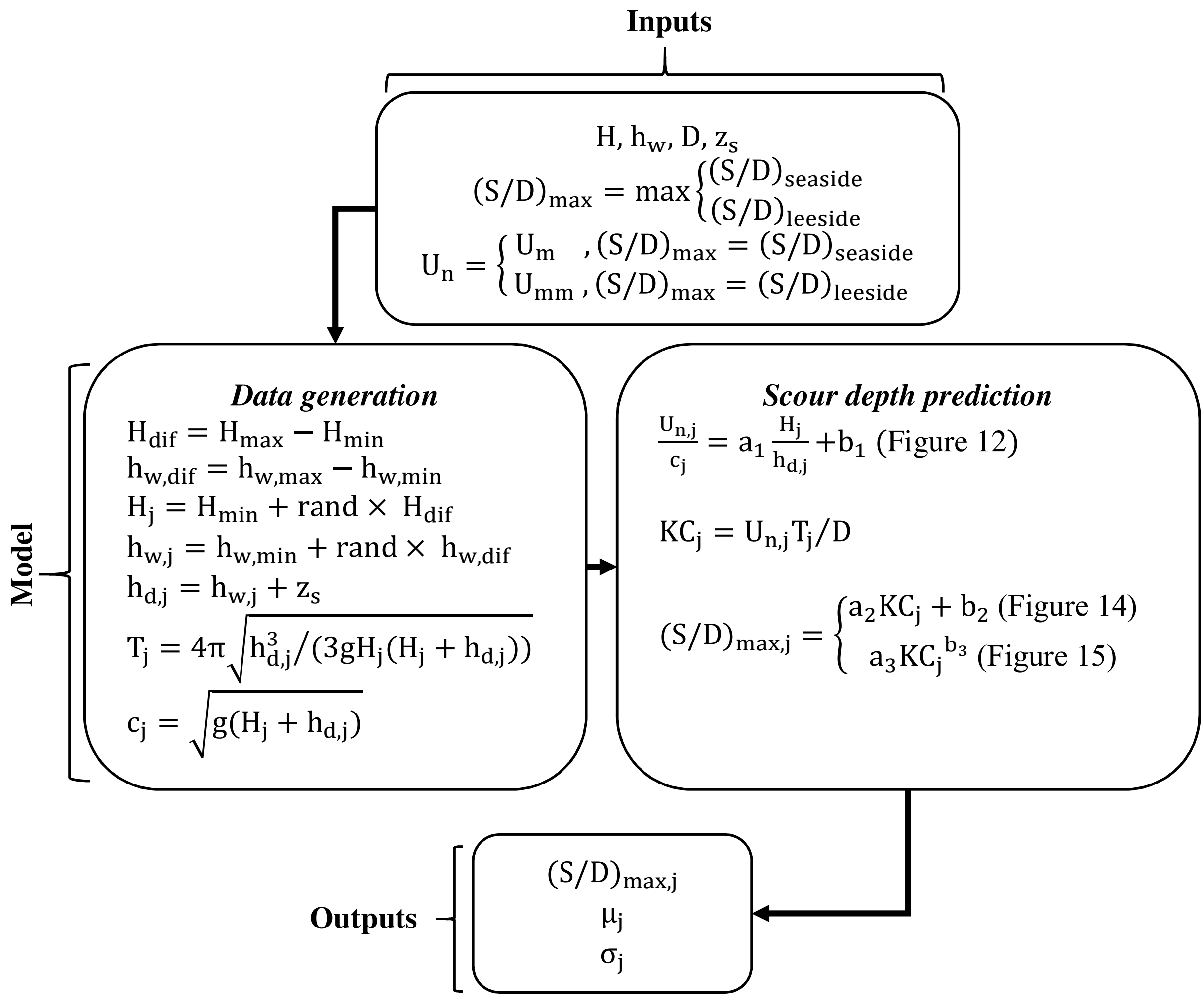

Figure 13: Structure of Monte Carlo model for scour depth $(S/D)_{max,j}$, μ_j and σ_j are mean and standard deviation, respectively. a_1, a_2, a_3 and b_1, b_2, b_3 are constants obtained via curve-fitting exercise. rand is the uniformly distributed random number ranging between 0 to 1. j indicates each value from population. z_s is thickness of sandy berm.

The mean (μ) and standard deviation (σ) are used as the metrics to quantify the degree of variation of $(S/D)_{max}$ with changes in the structure dimension and layout (Figure 14). The mean and standard deviation are calculated from the Gaussian distribution which fits well to the probability distribution of the simulated scour depths. The analysis shows a difference of less than 20% between the mean scour depths of the two layouts, for a given structure dimension. A greater magnitude of μ is obtained for the side layout. Furthermore, the magnitude of μ for the larger structure is found to be ~36% greater than the one for the smaller structure, irrespective of the layout. This may indicate that $(S/D)_{max}$ is more sensitive to the structure dimension than the layout.

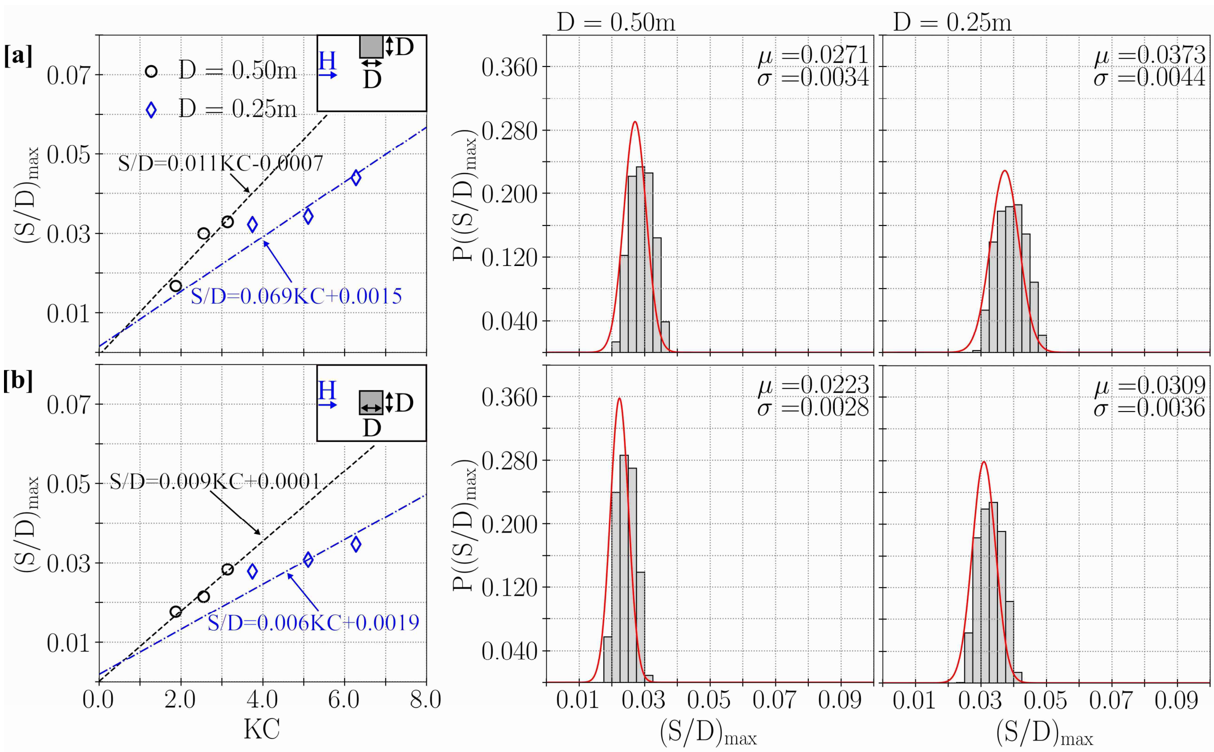

Figure 14: Variation of $(S/D)_{max}$ with respect to KC for: [a] side layout; [b] center layout, for smaller and larger structure, separately. Red solid curve indicates probability density function (PDF)

To quantify the variation of $(S/D)_{max}$ with respect to the layout, the empirical relationships and corresponding statistical properties are established, similar to those above (Figure 15 - [a] and [b]). The difference between the magnitudes of μ for the two layouts is ~15%. Furthermore, a generic relationship for the maximum dimensionless scour depth encompassing the two structure dimensions and layouts is established as shown in Figure 15-[c]. When the two layouts are combined, the μ values deviate nearly 9% and 5% from those of the cases with side and center layouts, respectively (Figure 15 - [c]).

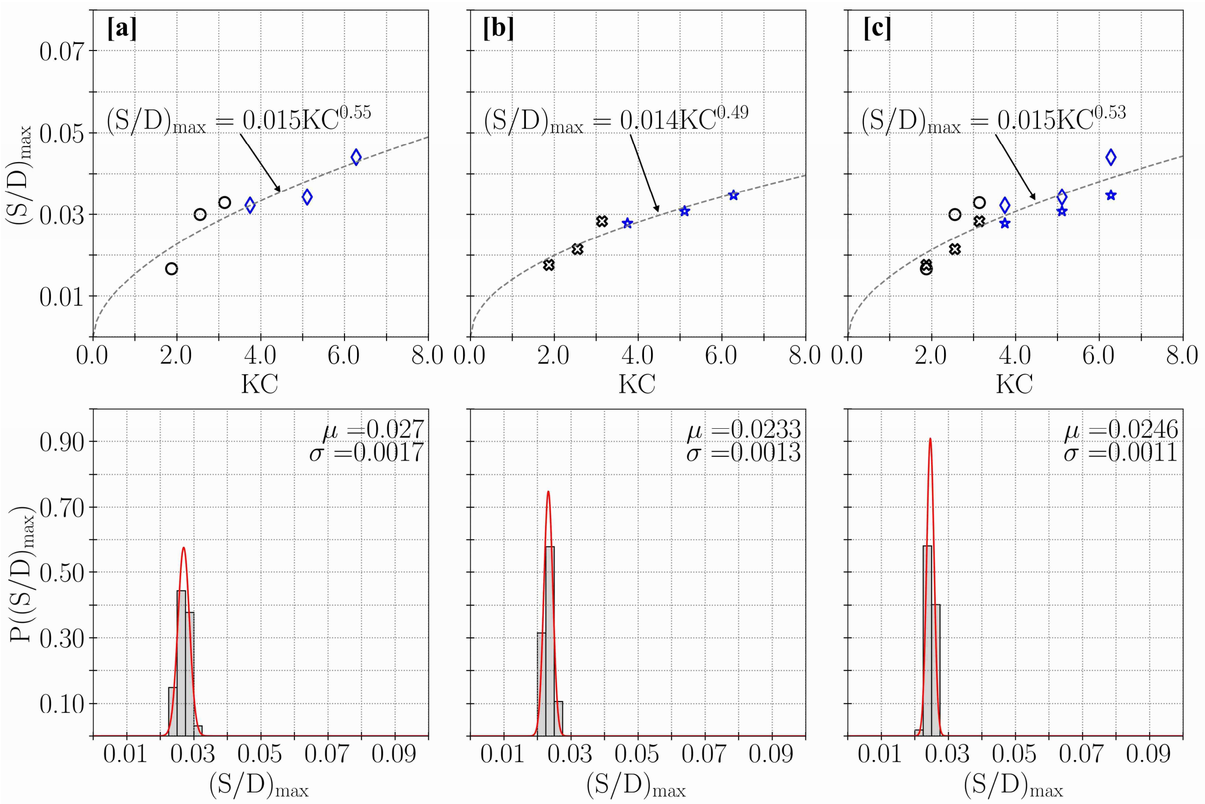

Figure 15: Variation of $(S/D)_{max}$ with respect to KC for [a] side layout [b] center layout [c] for two structure dimensions combined. Circles and crosses represent the structure dimension D=0.50 m; diamonds and stars represent the structure dimension D=0.25 m. Red solid curve indicates probability density function (PDF)

5.5. Numerical Model Results

Figure 16 depicts the plan views of the surface horizontal velocity ($U = \sqrt{u^2 + v^2}$) as well as the vertical velocity component (w) at two different depths, $h_w/3$ above the sandy berm (z_1) and on the surface of the sandy berm (z_2). The figure also shows the normalized bathymetric changes at various time instants. Furthermore, the cross-sectional views of the volumetric sediment concentration (ϕ_s) are illustrated for the same time instants. As the incident wave approaches the structure, the flow velocity is significantly intensified especially near the edges, which results in a lateral pressure gradient. Soon after the wave impinges on the structure, a vortex forms at the edge of the structure due to the flow separation. Upon the formation of this out-of-plane vortex, the strongest surface horizontal velocities are detected close to the vortex core, and the intensity of U reduces with the increase of the water depth (t = 7 s). Furthermore, the circular pattern of U at

$t = 7$ s stipulates that the vortex width is reduced with the depth. Even though at the core of the vortex at z_1 the flow is downward-directed (w<0), near the bed at z_2, an upward-directed flow forms (w>0), which may enhance the sediment suspension. Contrary to U and w at z_2, the surface horizontal and vertical velocities at z_1 intensify as the wake vortex propagates along its spiral trajectory, $t = 8$ s. However, the similar intensities of U and w at z_2 at two different time instants ($t = 7$ s and $t = 8$ s) indicate that the sediment suspension does not necessarily need to be affected by the fluctuations in the vortex intensity above the bed. Furthermore, as the wake vortex drifts further seaward, it can no longer sustain its energy and starts to dissipate, $t = 9$ s – 11 s, leaving the sediment deposits along the vortex trajectory.

The cross-sectional views of ϕ_s at four different locations show that the sediment brought in motion by the vortex-induced vertical velocity at z_2 is entrapped by the vortices. However, the temporal variations of ϕ_s indicate that the suspended sediment transport is confined mostly between $z =$ -0.3 m and $z =$-0.24 m. This can be related to a the underprediction of the vertical velocity, w, by the model which is unable to predict the suspended sediment further upward to z_1. Thus, the suspended sediments, especially in the vicinity of the wake vortex, are relatively non-existent as the near-bed w vanishes ($t = 11$ s). Furthermore, the SedWaveFoam model predicts sediment deposits on the downstream sides of the scour holes (Figure 7 – [c] and Figure 16 – [c]) contrary to the measurement (Figure 7 – [a]). This discrepancy is probably associated with the poor performance of the $\mathrm{k} - \varepsilon$ model which underpredicts the vertical velocity and thus the suspended load, yielding a higher bed load.

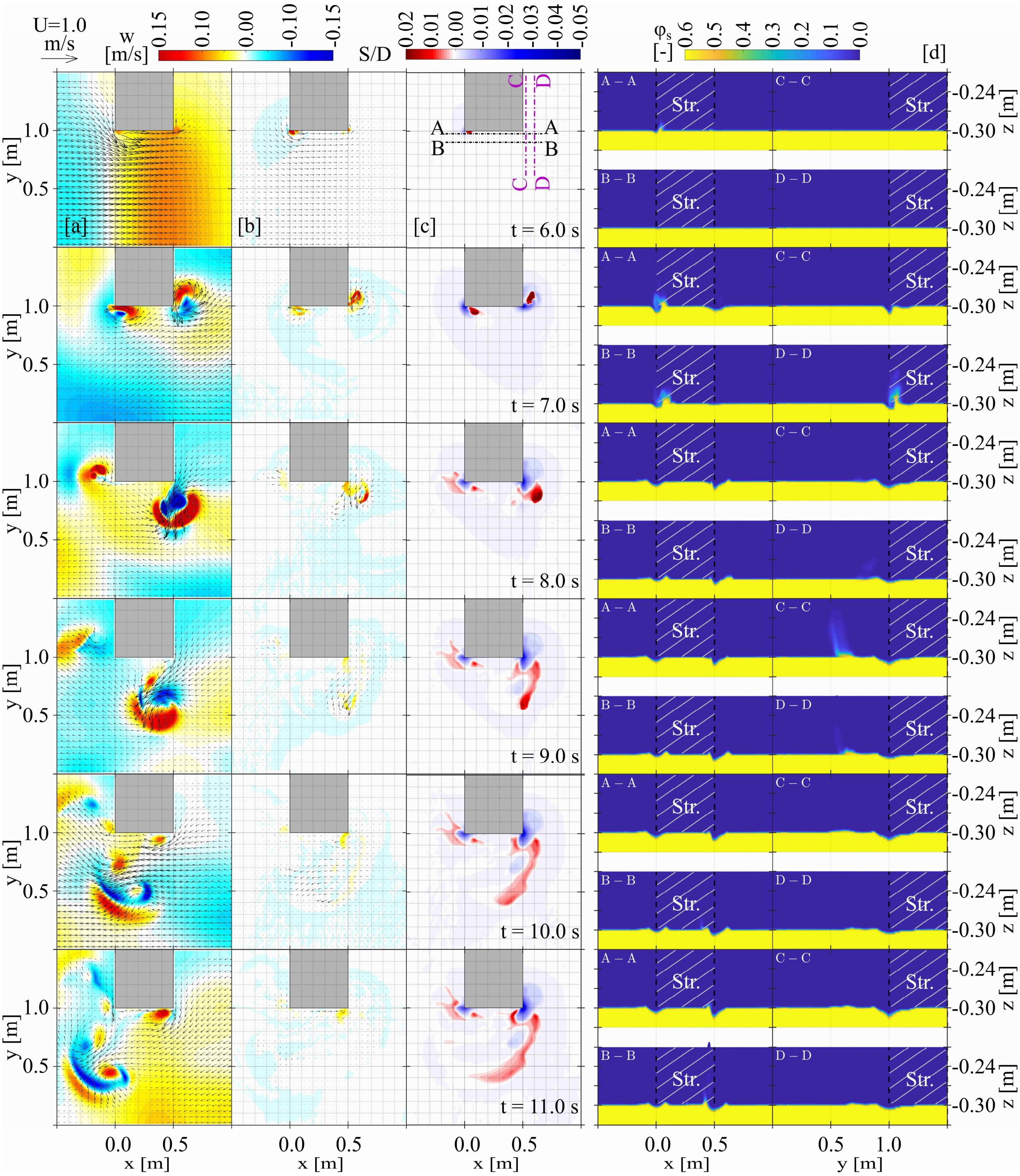

Figure 16: Plan views of [a, b] surface horizontal velocity (U) and vertical velocity component (w), and [c] bed elevation variation (S/D) for various time instants. [d] Cross-sectional views of normalized volumetric sediment concentration (ϕ_s) at various time instants. U and w shown in [a] and [b] are at $h_w/3$ above sandy berm, and on the surface of sandy berm, respectively.

Figure 17 illustrates the out-of-plane vorticity (ω_z) at the two depths, z_1 and z_2, as well as the 3D vortex tubes at various time instants. In Figure 17 – [a, b], the positive and negative vorticities indicate the vortex duplet, one rotating counterclockwise (CCW), and the other clockwise (CW), respectively. The vortex detection technique known as Q-criterion (Eq. 30), proposed by Hunt et al. (1988), is utilized to identify and visualize the 3D vortices.

$$Q = 0.5(|\Omega|^2 - |S|^2) \tag{30}$$

where Ω and S denote the symmetric and antisymmetric components of the velocity tensor, respectively. Here, Q = 5, 7.5, and 10 are adapted for better visualization of the primary vortex tubes.

The intensity of ω_z ranging between – 30 Hz and + 30 Hz proves that the wake vortices (ω_{zb}) are greater in size and more intense compared to the out-of-plane vortices on the seaside of the structure (ω_{za}) at the two selected depths. The relative positions of the CCW rotating out-of-plane vortices at different time instants follow a spiral trajectory (t = 7 s – 11 s). Furthermore, the relative difference in the intensities of U along the water column suggests that the out-of-plane vortices bend as they propagate. This phenomenon is more apparent in the wake vortex. The plan views of ω_z at t = 11 s illustrate that the vortex dissipates more rapidly at z_2 than z_1—the dissipation is initiated at the bed and expands to the surface. The offshore-directed flow which leads to the formation of CW rotating vortices, ω'_{za} and ω'_{zb}, next to ω_{za} and ω_{zb} is attributed to the water surface depression following the wave crest (Figure 5).

The Q-criterion plots show that the turbulence-averaged vortex tubes on both sides of the structure are approximately cylindrical and extend throughout the water column. These obliquely oriented vortex tubes are attributed to the relative vertical gradient of U as noted earlier. As the vortices duplet spin in opposite directions and propagate along the spiral trajectories, they become separated. The comparisons of the Q-criterion plots for the three different Q values also indicate that the wake vortex (ω_{zb}) is the strongest vortex among the others, as noted earlier.

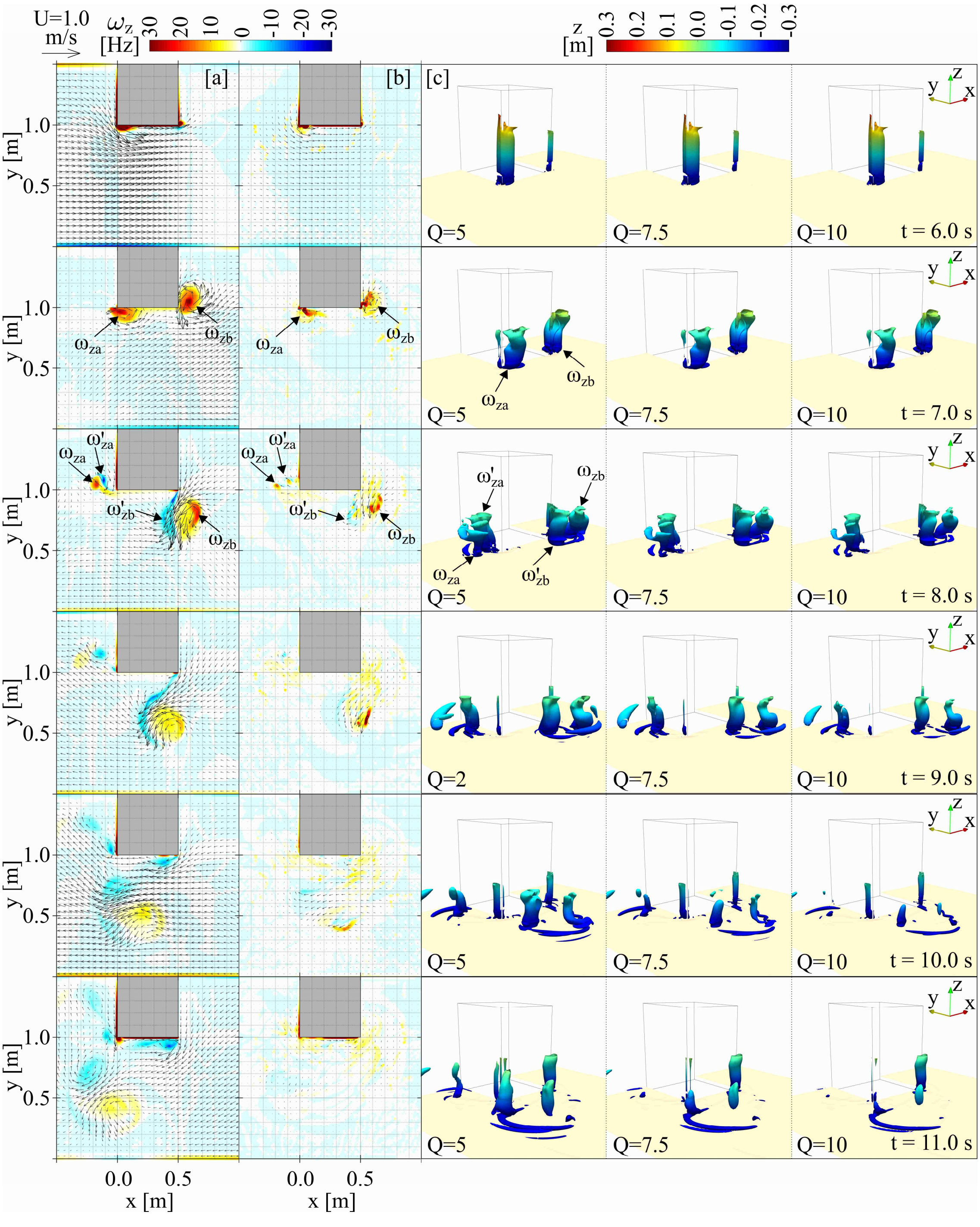

Figure 17: Plan views of [a, b] out-of-plane vorticity (ω_z) and [c] Q-criterion plots for various time instants. ω_z shown in [a] and [b] are at $h_w/3$ from sandy berm, and on the surface of sandy berm, respectively. Q = 5, 7.5 and 10.

6.CONCLUSIONS

This paper presents the results of experimental and numerical investigations of the characteristics of the solitary wave-induced scour around non-slender, vertical structures of square cross-section. The solitary wave boundary layer over the hydraulically transitional sandy berm is laminar in all test cases.

The analyses of the experimental data show that S/D, characterized as a function of KC, increases with KC more rapidly on the seaside than the leeside, irrespective of the structure dimension or layout. On the other hand, the scour's average width and volume increase with KC more rapidly on the leeside than the seaside. The primary cause of such phenomena is the higher bottom shear stress on the leeside corner of the structure, which is associated with the flow modification and the formation of larger eddies due to the flow blockage. Most of the sediments deposited near the structure are likely supplied from the material on leeside corner of the structure. Once the Shields parameter exceeds the threshold value, the sediment is brought into suspension, entrapped, and transported by the wake vortices up to a distance nearly equal to the structure dimension. Thus, the main driving mechanism of the scour around the structures is identified as the wake vortices. It is found that, for a given KC, deeper and wider scour holes are created when the structure dimension is larger, regardless of the layout. Although the structure dimension appeared to be a more important parameter than the layout for the maximum scour depth, the variation of the mean values of the maximum scour depths for all dimensions and layouts combined, deviate approximately 9% and 5% from those of the side and center layouts, respectively.

The numerical analysis carried out using SedWaveFoam shows that the mesh size is more critical for predicting the bed evolution than the flow field. As the incident wave approaches the structure, the intensified flow field near the sharp edges induces lateral pressure gradients leading to flow separations and the formation of vortices at the edges. The strongest surface horizontal velocity can be detected at the vortex core. The two-dimensional counterclockwise rotating out-of-plane vortices evolve into 3D cylindrical vortex tubes that extend throughout the water column. The gradient of the surface horizontal velocity along the water column; however, deforms these cylindrical vortices to obliquely oriented vortex tubes as they propagate along the spiral trajectories.

The main sediment transport mode is determined as the vortex-induced suspended sediment transport, confined within the lowest 20% of the water column. Overall, the SedWaveFoam model is found to be well-suited for simulating scours around non-slender structures and bed evolution under low Keulegan–Carpenter number flow conditions.

The findings of the present study are limited to the flow conditions and structure sizes considered. A more comprehensive study encompassing a wider range of flow conditions, layouts, and structure dimensions needs to be undertaken for conclusive analyses of scour around non-slender structures by wave actions.

Acknowledgments

This study was funded by The New York State Energy Research and Development Authority (NYSERDA) under agreement No. 105162, The New York State Department of Environmental Conservation, under Award No. 77362, and National Oceanic and Atmospheric Administration, New York Sea Grant, Award No. 80794. The authors would like to thank the funding agencies for their support.

REFERENCES

Baykal, C., Sumer, B.M., Fuhrman, D.R., Jacobsen, N.G., Fredsøe, J., 2017. Numerical simulation of scour and backfilling processes around a circular pile in waves. Coastal Engineering 122, 87–107. https://doi.org/10.1016/j.coastaleng.2017.01.004

Berberović, E., van Hinsberg, N.P., Jakirlić, S., Roisman, I. V, Tropea, C., 2009. Drop impact onto a liquid layer of finite thickness: Dynamics of the cavity evolution. Physical Review E 79, 36306. https://doi.org/https://doi.org/10.1103/PhysRevE.79.036306

Breusers, H.N.C., Nicollet, G., Shen, H.W., 1977. Local scour around cylindrical piers. Journal of Hydraulic Research 15, 211–252.

Carstensen, S., Sumer, B.M., Fredsøe, J., 2010. Coherent structures in wave boundary layers. Part 1. Oscillatory motion. Journal of Fluid Mechanics. https://doi.org/10.1017/S0022112009992825

Chauchat, J., Cheng, Z., Nagel, T., Bonamy, C., Hsu, T.J., 2017. SedFoam-2.0: A 3-D two-phase flow numerical model for sediment transport. Geoscientific Model Development 10, 4367–4392. https://doi.org/https://doi.org/10.5194/gmd-10-4367-2017

Ding, J., Gidaspow, D., 1990. A bubbling fluidization model using kinetic theory of granular flow. AIChE journal 36, 523–538.

Drew, D.A., 1983. Mathematical modeling of two-phase flow. Annual review of fluid mechanics 15, 261–291.

Fredsøe, J., 1984. Turbulent boundary layer in wave-current motion. Journal of Hydraulic Engineering. https://doi.org/10.1061/(ASCE)0733-9429(1984)110:8(1103)

Fredsøe, J., Deigaard, R., 1992. Mechanics of coastal sediment transport. World Scientific.

Fuhrman, D.R., Fredsøe, J., Sumer, B.M., 2009a. Bed slope effects on turbulent wave boundary layers: 2. Comparison with skewness, asymmetry, and other effects. Journal of Geophysical Research: Oceans. https://doi.org/10.1029/2008JC005053

Fuhrman, D.R., Fredsoe, J., Sumer, B.M., 2009b. Bed slope effects on turbulent wave boundary layers: 1. Model validation and quantification of rough-turbulent results. Journal of Geophysical Research: Oceans. https://doi.org/10.1029/2008JC005045

Fuhrman, D.R., Schløer, S., Sterner, J., 2013. RANS-based simulation of turbulent wave boundary layer and sheet-flow sediment transport processes. Coastal Engineering 73, 151–166. https://doi.org/10.1016/j.coastaleng.2012.11.001

Goseberg, N., Schlurmann, T., 2012. Interaction of Idealized Urban Infrastructure and Long Waves During Run-up and On-land Flow Process in Coastal Regions. Coastal Engineering Proceedings.

Goseberg, N., Schlurmann, T., 2011. Numerical and Experimental Study on Tsunami Run-Up and Inundation Influenced By Macro Roughness Elements. Coastal Engineering Proceedings. https://doi.org/10.9753/icce.v32.currents.13

Haddorp, R., 2005. Predictability of Scour at Large Piles due to Waves and Currents.

Henderson, S.M., Allen, J.S., Newberger, P.A., 2004. Nearshore sandbar migration predicted by an eddy-diffusive boundary layer model. Journal of Geophysical Research: Oceans 109. https://doi.org/https://doi.org/10.1029/2003JC002137

Hsu, T.-J., Hanes, D.M., 2004. Effects of wave shape on sheet flow sediment transport. Journal of Geophysical Research: Oceans 109.

Huang, Z., Yuan, Z., 2010. Transmission of solitary waves through slotted barriers: A laboratory study with analysis by a long wave approximation. Journal of Hydro-Environment Research. https://doi.org/10.1016/j.jher.2009.10.009

Hunt, J.C.R., Wray, A.A., Moin, P., 1988. Eddies, streams, and convergence zones in turbulent flows.

Isaacson, M., 1979. Wave-induced forces in the diffraction regime. Mechanics of wave-induced forces on cylinders.

Jacobsen, N.G., Fuhrman, D.R., Fredsøe, J., 2012. A wave generation toolbox for the open-source CFD library: OpenFoam®. International Journal for Numerical Methods in Fluids 70, 1073–1088. https://doi.org/https://doi.org/10.1002/fld.2726

Jenkins, J.T., Savage, S.B., 1983. A theory for the rapid flow of identical, smooth, nearly elastic, spherical particles. Journal of Fluid Mechanics. https://doi.org/10.1017/S0022112083001044

Katsui, H., Toue, T., 1993. Scouring around a Large Scale Offshore Structure. Doboku Gakkai Ronbunshu 1993, 73–82.

Katsui, H., Toue, T., 1989. Inception of sand motion around a large obstacle, in: Coastal Engineering 1988. pp. 1280–1294.

Katsui, H., Toue, T., others, 1993. Methodology of estimation of scouring around large-scale offshore structures, in: The Third International Offshore and Polar Engineering Conference.

Kim, C.-J., Iwata, K., Miyaike, Y., Yu, H.-S., 1995. Topographical change around multiple large cylindrical structures under wave actions, in: Coastal Engineering 1994. pp. 1212–1226.

Kim, Y., Cheng, Z., Hsu, T.-J., Chauchat, J., 2018. A numerical study of sheet flow under monochromatic nonbreaking waves using a free surface resolving Eulerian two-phase flow model. Journal of Geophysical Research: Oceans 123, 4693–4719.

Kobayashi, T., 1993. 3-d analysis of flow around a vertical cylinder on a scoured bed, in: Proceedings of the Coastal Engineering Conference. https://doi.org/10.1061/9780872629332.264

Kobayashi, T., Oda, K., 1995. Experimental study on developing process of local scour around a vertical cylinder, in: Proceedings of the Coastal Engineering Conference. https://doi.org/10.1061/9780784400890.094

Kranenburg, W.M., Ribberink, J.S., Schretlen, J.J.L.M., Uittenbogaard, R.E., 2013. Sand transport beneath waves: The role of progressive wave streaming and other free surface effects. Journal of Geophysical Research: Earth Surface 118, 122–139. https://doi.org/https://doi.org/10.1029/2012JF002427

Kranenburg, W.M., Ribberink, J.S., Uittenbogaard, R.E., Hulscher, S.J.M.H., 2012. Net currents in the wave bottom boundary layer: On waveshape streaming and progressive wave streaming. Journal of Geophysical Research: Earth Surface 117. https://doi.org/https://doi.org/10.1029/2011JF002070

McGovern, D.J., Todd, D., Rossetto, T., Whitehouse, R.J.S., Monaghan, J., Gomes, E., 2019. Experimental observations of tsunami induced scour at onshore structures. Coastal Engineering 152, 103505.

Menter, F., Esch, T., 2001. Elements of industrial heat transfer predictions, in: 16th Brazilian Congress of Mechanical Engineering (COBEM). p. 650.

Menter, F.R., Kuntz, M., Langtry, R., 2003. Ten years of industrial experience with the SST turbulence model. Turbulence, heat and mass transfer 4, 625–632.

Nakamura, T., Kuramitsu, Y., Mizutani, N., 2008. Tsunami scour around a square structure. Coastal engineering journal 50, 209–246.

Pope, S.B., 2001. Turbulent Flows. Measurement Science and Technology. https://doi.org/10.1088/0957-0233/12/11/705

Qi, W.-G., Gao, F.-P., 2014. Physical modeling of local scour development around a large-diameter monopile in combined waves and current. Coastal Engineering 83, 72–81.

Raaijmakers, T., Rudolph, D., 2008. Time-dependent scour development under combined current and waves conditions-laboratory experiments with online monitoring technique, in: Proc. 4th Int. Conf. Scour Erosion, ICSE, Tokyo. pp. 152–161.

Rance, P.J., 1980. The potential for scour around large objects. Scour prevention techniques around offshore structures 41–53.

Rodi, W., 1993. Turbulence models and their application in hydraulics. CRC Press. https://doi.org/10.1016/0045-7825(81)90171-7

Saito, E., Sato, S., Shibayama, T., 1991. Local scour around a large circular cylinder due to wave action, in: Coastal Engineering 1990. pp. 1795–1804.

Saito, E., Shibayama, T., 1993. Local Scour Around a Large Circular Cylinder on the Uniform Bottom Slope Due to Waves and Currents, in: Coastal Engineering 1992. pp. 2799–2810.

Sogut, E., Farhadzadeh, A., 2020. Scouring and Loading of Idealized Beachfron Building During Overland Flooding. Coastal Engineering Proceedings 7.

Sogut, E., Velioglu Sogut, D., Farhadzadeh, A., 2020. Overland Wave Propagation and Load Distribution among Arrays of Elevated Beachfront Structures. Journal of Waterway, Port, Coastal, and Ocean Engineering 146, 04020016. https://doi.org/10.1061/(ASCE)WW.1943-5460.0000579

Sogut, E., Velioglu Sogut, D., Farhadzadeh, A., 2019. Effects of building arrangement on flow and pressure fields generated by a solitary wave interacting with developed coasts. Advances in Water Resources 134, 103450. https://doi.org/10.1016/j.advwatres.2019.103450

Soulsby, R., 1997. Dynamics of marine sands: a manual for practical applications. Thomas Telford.

Soulsby, R.L., Whitehouse, R.J.S., 1997. Threshold of sediment motion in coastal environments. Proceedings Pacific Coasts and Ports 1997 Conference.

Sumer, B.M., Christiansen, N., Fredsøe, J., 1997. The horseshoe vortex and vortex shedding around a vertical wall-mounted cylinder exposed to waves. Journal of Fluid Mechanics. https://doi.org/10.1017/s0022112096003898

Sumer, B.M., Christiansen, N., Fredsøe, J., 1993. Influence of cross section on wave scour around piles. Journal of Waterway, Port, Coastal and Ocean Engineering. https://doi.org/10.1061/(ASCE)0733-950X(1993)119:5(477)

Sumer, B.M., Christiansen, N., Fredsoe, J., 1992. Time scale of scour around a vertical pile, in: The Second International Offshore and Polar Engineering Conference. International Society of Offshore and Polar Engineers.

Sumer, B.M., Fredsøe, J., 2002. The mechanics of scour in the marine environment, Adv. Ser. Ocean Eng 17.

Sumer, B.M., Fredsøe, J., 2001. Wave scour around a large vertical circular cylinder. Journal of waterway, port, coastal, and ocean engineering 127, 125–134.

Sumer, B.M., Fuhrman, D.R., 2020. Turbulence in coastal and civil engineering, in: Advanced Series on Ocean Engineering. https://doi.org/10.1142/9789813234314_fmatter

Sumer, B.M., Hatipoglu, F., Fredsøe, J., 2007. Wave scour around a pile in sand, medium dense, and dense silt. Journal of Waterway, Port, Coastal and Ocean Engineering. https://doi.org/10.1061/(ASCE)0733-950X(2007)133:1(14)

Sumer, B.M., Jensen, P.M., Sørensen, L.B., Fredsøe, J., Liu, P.L.F., Carstensen, S., 2010. Coherent structures in wave boundary layers. Part 2. Solitary motion. Journal of Fluid Mechanics. https://doi.org/10.1017/S0022112009992837

Toue, T., Katsui, H., Nadaoka, K., 1993. Mechanism of sediment transport around a large circular cylinder, in: Coastal Engineering 1992. pp. 2867–2878.

Velioglu Sogut, D., Sogut, E., Farhadzadeh, A., 2021. Interaction of a solitary wave with an array of macro-roughness elements in the presence of steady currents. Coastal Engineering 164, 103829. https://doi.org/10.1016/j.coastaleng.2020.103829

Whitehouse, R., 1998. Scour at marine structures: A manual for practical applications. Thomas Telford.

Whitehouse, R.J.S., 2004. Marine scour at large foundations, in: Proceedings of the Second International Conference on Scour and Erosion. Singapore, pp. 455–463.

Wilcox, D.C., 1998. Turbulence modeling for CFD. DCW industries La Canada, CA.

Xu, C., Huang, Z., Yao, Y., 2019. A wave-flume study of scour at a pile breakwater: Solitary waves. Applied Ocean Research. https://doi.org/10.1016/j.apor.2018.10.026

Zanke, U.C.E., Hsu, T.-W., Roland, A., Link, O., Diab, R., 2011. Equilibrium scour depths around piles in noncohesive sediments under currents and waves. Coastal Engineering 58, 986–991.